Multiscale geometric analysis of turbulence by curvelets

Jianwei Ma,[1] M. Yousuff Hussaini,[2] Oleg V. Vasilyev,[3] and Francois-Xavier Le Dimet[4]
[1]*School of Aerospace, Tsinghua University, Beijing 100084, China*
[2]*School of Computational Science, Florida State University, Tallahassee, Florida 32306, USA*
[3]*Department of Mechanical Engineering, University of Colorado, Boulder, Colorado 80309, USA*
[4]*Laboratory Jean-Kuntzman, Université de Grenoble and INRIA, BP 53, 38041 Grenoble Cedex 9, France*

(Received 18 February 2009; accepted 6 June 2009; published online 22 July 2009)

In this paper, after a brief review of curvelets and their relation to classical wavelet transform, multiscale geometric analysis is systematically applied to turbulent flows in two and three dimensions. The analysis is based on the constrained minimization of a total variation functional representing the difference between the data and its representation in the curvelet space. Constrained multiscale minimization results in a minimum loss of the geometric flow features and the extraction of the coherent structures with their edges and geometry properly preserved, which is significant for turbulence modeling. The effectiveness of curvelet analysis compared to the wavelet transform is demonstrated for both two- and three-dimensional turbulent flows. © *2009 American Institute of Physics*. [DOI: 10.1063/1.3177355]

I. INTRODUCTION

The objective of organizing, representing, and manipulating high-dimensional data with a view to detect significant features that occupy lower-dimensional subsets (curves, sheets, etc.) has been pursued independently by mathematical and statistical analysts and computer vision and image scientists. Recently, there has been an attempt to bring together these theories and tools, which are closely related and application driven, into an emerging area called multiscale geometric analysis (MGA). MGA techniques have the potential to make considerable advances in science and engineering areas where multiscale phenomena are of critical interest.

Turbulence has been a source of fascination for centuries because most fluid flows occurring in nature, as well as in engineering applications, are turbulent. Fluid turbulence is a paradigm of multiscale phenomena, where the coherent structures evolve in an incoherent random background. From a mathematical point of view, the geometrical representation of flow structures might seem restricted to a well-defined set of curves along which the data are singular. As a consequence, the efficient compression of a flow field with minimum loss of the geometric flow structures is a crucial problem in the simulation of turbulence. Multiscale geometric techniques addressed in this paper are beginning to influence the field of turbulence and have the potential to upstage the wavelet representation of turbulent flows.

Despite tremendous progress in the area of scientific computing, the direct numerical simulation (DNS) of turbulent flows using first principles is prohibitively expensive, if not impossible, even on petascale platforms. Approaches such as large-eddy simulation (LES)[1–3] and multiscale modeling[4–6] have recently become popular for the computation of complex turbulent flows. These methods use either filtering or a projection operator to separate resolved (large/coherent/energetic) and unresolved (small/incoherent/low energy) modes. The motivation is based on the observed fact that the large scale or energy containing motions often dominate mixing, heat transfer, and other quantities of engineering interest, while the small scale or low energy eddies are only of interest because of how they affect the resolved modes. Therefore, the extraction and separation of coherent (dynamically dominant) and incoherent (dynamically insignificant) structures from turbulent flow fields is critical if one needs to capture the "important" flow physics, improve the fidelity of the approach, simplify the complexity of the subgrid scale (SGS) models, and reduce computational cost.

The multiscale separation concepts based on nonlinear wavelet denoising were proposed by Farge and co-workers (see, e.g., Refs. 7–10). Specifically, they proposed a wavelet-based coherent vortex simulation (CVS) approach based on thresholding of orthogonal wavelet decompositions. They observed that the coherent flow component is highly concentrated in wavelet space, which contains most of the total energy and enstrophy of the original flow. In the original formulation, the CVS decomposes the turbulent vorticity field into resolved coherent eddies and the residual field that is close to incoherent Gaussian noise. The evolution of the coherent field is then computed deterministically while neglecting or modeling the effect of the incoherent noise. The original formulation was extended to wavelet packets,[10,11] biorthogonal wavelets,[12] and second-generation wavelets.[13] Recently, the CVS approach was further generalized into the stochastic coherent adaptive LES (SCALES)[5,13] methodology that "tracks" on a space-time adaptive mesh the most energetic (dynamically dominant) coherent structures while modeling the influence of the unresolved motions.

Although applications of wavelets to turbulent flows have become increasingly popular, traditional wavelets perform well only at representing point singularities since they ignore the geometric properties of structures and do not exploit the regularity of edges. Therefore, wavelet-based compression and structure extraction becomes computationally inefficient for geometric features with line and surface singularities. Discrete wavelet thresholding could lead to oscil-

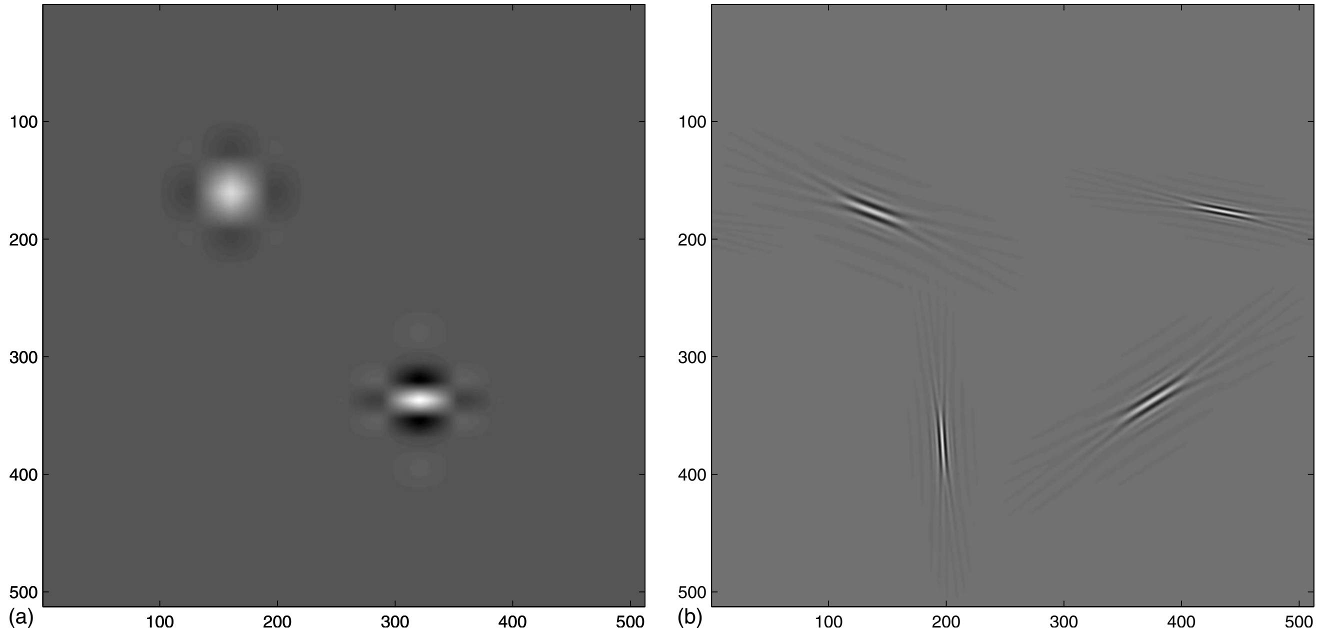

FIG. 1. The elements of wavelets (left) and curvelets on various scales, directions, and translations in the spatial domain (right). Note that the tensor-product 2D wavelets are not strictly isotropic but have directional selectivity.

lations along the edges of coherent eddies and, consequently, to the deterioration of the vortex tube structures, which, in turn, can lead to an unphysical leak of energy into neighboring scales producing an artificial "cascade" of energy.[14]

A multiresolution geometric analysis, named curvelet transform, was first proposed by Candès and Donoho[15] based on block ridgelets, and then the second generation was constructed based on the frequency partition in Refs. 16 and 17. In two dimensions, the curvelet transform allows an optimal sparse representation of objects with C^2-singularities. For a smooth object f with discontinuities along C^2-continuous curves, the best m-term approximation $\tilde{f}_m$ by curvelet thresholding obeys $\|f-\tilde{f}_m\|_2^2 \leq Cm^{-2}(\log m)^3$, while for wavelets the decay rate is only m^{-1}. Surprising performance has been shown in the field of image processing (see, e.g., Refs. 18–22). Recently, the three-dimensional (3D) curvelet transform was presented by Candès and co-workers.[17,23] Unlike the isotropic elements of wavelets, the needle-shaped elements of this transform possess very high directional sensitivity and anisotropy [see Fig. 1 for the two-dimensional (2D) case]. Such an element is very efficient in representing vortex edges.

Very recently, the curvelet transform has been independently applied to the analysis of 3D turbulence by Ma and Hussaini[24] and Bermejo-Moreno and Pullin.[25] A multiscale methodology for the study of the nonlocal geometry of eddy structures in turbulence was developed. The multiscale property, implemented by means of curvelets, provides the framework for studying the evolution of the structures associated with the main ranges of scales defined in Fourier space while keeping the localization in physical space that enables a geometrical study of such structures. Such a geometrical characterization could provide improved understanding of cascade mechanics and dissipation-range dynamics, contributing potentially to the development of structure-based models of turbulence fine scales, SGS models for LES, and simulation methods based on *priori* wavelet transforms.

The main difference between the results reported in Refs. 24 and 25 is that the main focus of Ma and Hussaini[24] is the extraction of coherent vortices out of 3D turbulent flows by curvelet shrinkage with the objective to propose an alternative method to the existing wavelet methods of coherent vortex analysis, while the main focus of the methodology presented in Ref. 25 is the analysis of nonlocal geometrical structures by combining the curvelets with statistical and clustering techniques. The methodology reported in Ref. 25 involves three steps: extraction, characterization, and classification of structures from a given 3D turbulent field. The extraction step consists of two stages: multiscale decomposition and isocontouring of each component at different scales. The curvelet transform was used in the first stage that decomposes the fields into multiscale and multiorientation components. The motivation of Bermejo-Moreno and Pullin[25] is to develop a methodology that can compensate for the computational bottleneck of DNS computing for turbulent flows and to provide a mathematical framework for nonlocal characterization of the flow structures based on the existing data sets.

This paper is an extension of Ref. 24. We investigate systematically the applications of curvelets for the extraction of coherent vortices from 2D to 3D turbulent flows. More details and results are provided. Besides the extension, we propose a new scheme of curvelet shrinkage for the extraction by using the second-generation discrete curvelet transform (DCuT) combined with a total variation (TV) minimization. This TV-synthesis curvelet shrinkage can reduce pseudo-Gibbs and elementlike artifacts while preserving the geometric structures in extracted fields, in comparison with classical hard-thresholding or soft-thresholding methods. The aim of this paper is to propose an updated multiscale geometric analysis tool for the existing wavelet methods in the fluid mechanics community. We focus on comparisons of the proposed curvelet method and the popular wavelet transform from two dimensions to three dimensions.

In Sec. II a review of classical and geometric wavelets is given. The theory of 2D and 3D curvelet transforms is presented in Secs. III and IV, respectively. The application of curvelet shrinkage for the extraction of the coherent vortex out of turbulent flow is discussed in Sec. V. A uniform framework of TV minimization both for 2D and 3D curvelet transforms is given in Sec. VI. Experiments are shown from 2D to 3D turbulence in Sec. VII. Finally, conclusions are drawn in Sec. VIII.

II. CLASSICAL TO GEOMETRIC WAVELETS

Although the discrete wavelet transform (DWT) has established an impressive reputation as a tool for mathematical analysis and signal processing, it has the disadvantage of poor directionality, which has undermined its usage in many applications. Significant progress in the development of directional wavelets has been made in recent years. The complex wavelet transform (CWT) is one way to improve directional selectivity and only requires $O(N)$ computational cost. However, the CWT has not been widely used in the past due to the difficulty in designing complex wavelets with perfect reconstruction properties and good filter characteristics.[26,27] One popular technique is the dual-tree CWT proposed by Kingsbury,[28,29] which added perfect reconstruction to the other attractive properties of complex wavelets, including approximate shift invariance, six directional selectivities, limited redundancy, and efficient $O(N)$ computation.

The 2D complex wavelets are essentially still constructed by using tensor-product one-dimensional (1D) wavelets. The directional selectivity (six directions) is much better than classical DWT (three directions) but is still limited.

In 1999, an anisotropic geometric wavelet, named ridgelet, was proposed by Candès and co-worker.[30,31] The ridgelet transform is optimal at representing straight-line singularities. The transform with arbitrary directional selectivity provides a key to the analysis of higher-dimensional singularities. The main drawback of the ridgelet transform is the limitation of its applicability to objects with global straight-line singularities, which is rarely the case in real applications of image processing in industry.[32] In order to analyze local line or curve singularities, a natural idea is to apply a partition to the images and then apply the ridgelet transform to the partitioned subimages. This block ridgelet based transform, which is named curvelet transform, was first proposed by Candès and Donoho in 2000. Apart from the blocking effects, however, the application of the so-called first-generation curvelet transform is limited because the geometry of ridgelets is itself unclear, as they are not true ridge functions in digital images. In 2004, a considerably simpler second-generation curvelet transform based on a frequency partition technique was proposed by the same authors.

It should be noted that several other geometric multiresolution bases, such as wedgelets,[33] beamlets,[34] bandlets,[35,36] contourlets,[37] shearlets,[38] platelets,[39] and surfacelets,[40] have been proposed independently to identify and restore geometric features. The geometric wavelets are also called X-lets. From a mathematical point of view, the main strength of curvelets is their ability to formulate strong theorems in approximation and operator theory. On the other hand, curvelet-based multiscale geometric analysis has been contended by anisotropic diffusion filtering,[41] which is also related to MGA.

III. 2D CURVELET TRANSFORM

In this section, we give an outline for the second-generation DCuT,[16,17] which is considerably simpler to use than the original formulation.[15–17]

Let $V(t)$ and $W(r)$ be a pair of smooth, non-negative real-valued window functions, such that V is supported on $[-1,1]$ and W on $[\frac{1}{2},2]$. The windows need to satisfy the admissibility conditions

$$\sum_{l=-\infty}^{\infty} V^2(t-l)=1, \quad t\in\mathbb{R},$$

$$\sum_{j=-\infty}^{\infty} W^2(2^{-j}r)=1, \quad r>0.$$

These conditions are satisfied by taking, e.g., the scaled Meyer windows (see Ref. 42, p. 137)

$$V(t)=\begin{cases}1, & |t|\le 1/3,\\ \cos\left[\dfrac{\pi}{2}\nu(3|t|-1)\right], & 1/3\le|t|\le 2/3,\\ 0 & \text{else},\end{cases}$$

$$W(r)=\begin{cases}1, & 5/6\le r\le 4/3,\\ \cos\left[\dfrac{\pi}{2}\nu(5-6r)\right], & 2/3\le r\le 5/6,\\ \cos\left[\dfrac{\pi}{2}\nu(3r-4)\right], & 4/3\le r\le 5/3,\\ 0 & \text{else},\end{cases}$$

where ν is a smooth function satisfying

$$\nu(x)=\begin{cases}0, & x\le 0,\\ 1, & x\ge 1,\end{cases} \qquad \nu(x)+\nu(1-x)=1, \quad x\in\mathbb{R}.$$

Let the Fourier transform of $f\in L^2(\mathbb{R}^2)$ be defined by $\hat{f}(\boldsymbol{\xi}) \coloneqq 1/2\pi\int_{\mathbb{R}^2} f(x)e^{-i\langle x,\xi\rangle}d\boldsymbol{x}$. Now, for $j\ge 0$ let the window $U_j(\boldsymbol{\xi})$, $\boldsymbol{\xi}=(\xi_1,\xi_2)\in\mathbb{R}^2$ in frequency domain be given by

$$U_j(\boldsymbol{\xi})=2^{-3j/4}W(2^{-j}|\boldsymbol{\xi}|)V(2^{\lfloor j/2\rfloor}\theta), \quad \boldsymbol{\xi}\in\mathbb{R}^2,$$

where $(|\boldsymbol{\xi}|,\theta)$ denotes the polar coordinates corresponding to $\boldsymbol{\xi}$. The support of U_j is a polar wedge determined by supp $W(2^{-j}\cdot)=[2^{j-1},2^{j+1}]$ and supp $V(2^{\lfloor j/2\rfloor}\cdot)=[-2^{-\lfloor j/2\rfloor},2^{-\lfloor j/2\rfloor}]$ (see Fig. 2 for an example of the window U_0 and its support[19]).

The system of curvelets is now indexed by three parameters: a scale 2^{-j}, $j\in\mathbb{N}_0$; an equispaced sequence of rotation angles $\theta_{j,l}=2\pi l\cdot 2^{-\lfloor j/2\rfloor}$, $0\le l\le 2^{\lfloor j/2\rfloor}-1$; and a posi-

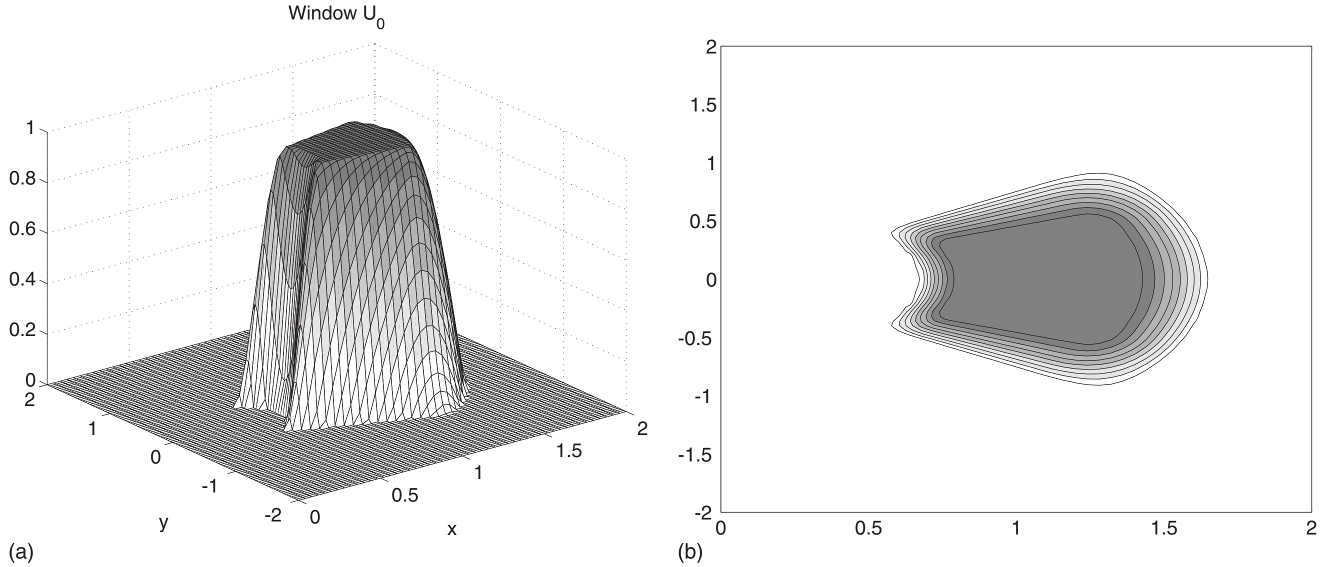

FIG. 2. Window $U_0(\boldsymbol{\xi})$ (left) and its support (right).

tion $\boldsymbol{x}_k^{(j,l)} = R_{\theta_{j,l}}^{-1}(k_1 2^{-j}, k_2 2^{-\lfloor j/2 \rfloor})^T$, $(k_1,k_2)\in\mathbb{Z}^2$, where $R_{\theta_{j,l}}$ denotes the rotation matrix with angle $\theta_{j,l}$. The curvelets are defined by

$$\varphi_{j,l,k}(\boldsymbol{x}) := \varphi_j[R_{\theta_{j,l}}(\boldsymbol{x}-\boldsymbol{x}_k^{(j,l)})], \quad \boldsymbol{x}=(x_1,x_2)\in\mathbb{R}^2,$$

where $\hat{\varphi}_j(\boldsymbol{\xi}) := U_j(\boldsymbol{\xi})$, i.e., U_j is the Fourier transform of φ_j. Observe that in the spatial domain $\varphi_{j,l,k}$ rapidly decays outside a 2^{-j} by $2^{-j/2}$ rectangle with center $\boldsymbol{x}_k^{(j,l)}$ and orientation $\theta_{j,l}$ with respect to the vertical axis. Further, we introduce the real-valued, non-negative low-pass window W_0 by

$$W_0(r)^2 + \sum_{j>0} W(2^{-j}r)^2 = 1,$$

with the coarse scale nondirectional curvelet given by

$$\varphi_{-1,0,k}(x) := \varphi_{-1}(\boldsymbol{x}-k), \quad \hat{\varphi}_{-1}(\boldsymbol{\xi}) := W_0(|\boldsymbol{\xi}|).$$

For simplification, let $\boldsymbol{\mu}=(j,l,k)$ be the collection of the triple index. The system of curvelets $(\varphi_{\boldsymbol{\mu}})$ forms a tight frame in $L^2(\mathbb{R}^2)$, i.e., each function $f\in L^2(\mathbb{R}^2)$ can be represented by

$$f = \sum_{\boldsymbol{\mu}} c_{\boldsymbol{\mu}}(f)\varphi_{\boldsymbol{\mu}}.$$

Using Parseval's identity, the curvelet coefficients are given by

$$c_{\boldsymbol{\mu}}(f) := \langle f,\varphi_{\boldsymbol{\mu}}\rangle = \int_{\mathbb{R}^2}\hat{f}(\boldsymbol{\xi})\overline{\hat{\varphi}_{\boldsymbol{\mu}}(\boldsymbol{\xi})}d\boldsymbol{\xi}$$

$$= \int_{\mathbb{R}^2}\hat{f}(\boldsymbol{\xi})\overline{U_j(R_{\theta_{j,l}}\boldsymbol{\xi})}e^{i\langle x_k^{(j,l)},\boldsymbol{\xi}\rangle}d\boldsymbol{\xi}. \quad (1)$$

In practical implementations, one would like to have Cartesian arrays instead of the polar tiling of the frequency plane. Cartesian coronas are based on concentric squares (instead of circles) and shears (see Fig. 3). Candès *et al.*[17] applied a pseudopolar grid by replacing the window $W_j(\boldsymbol{\xi}) := W(2^{-j}\boldsymbol{\xi})$ by a window of the form

$$\widetilde{W}_j(\boldsymbol{\xi}) = \chi_{[0,\infty)}(\xi_1)\sqrt{\phi^2(2^{-j-1}\xi_1)-\phi^2(2^{-j}\xi_1)}, \quad j\geq 0,$$

where the 1D window ϕ satisfies $0\leq\phi\leq 1$, supp $\phi\subset[-2,2]$, and $\phi(r)=1$ for $r\in[-1/2,1/2]$. [Here, $\chi_{[0,\infty)}(\xi_1)$ denotes the characteristic function of $[0,\infty)$.] As before, ϕ can be taken to be a scaled Meyer window.

With $V_j(\boldsymbol{\xi}) := V(2^{\lfloor j/2\rfloor}\xi_2/\xi_1)$ the Cartesian window,

$$\widetilde{U}_j(\boldsymbol{\xi}) := 2^{-3j/4}\widetilde{W}_j(\boldsymbol{\xi})V_j(\boldsymbol{\xi})$$

can be determined, being analogous to U_j and determining the frequencies near the wedge

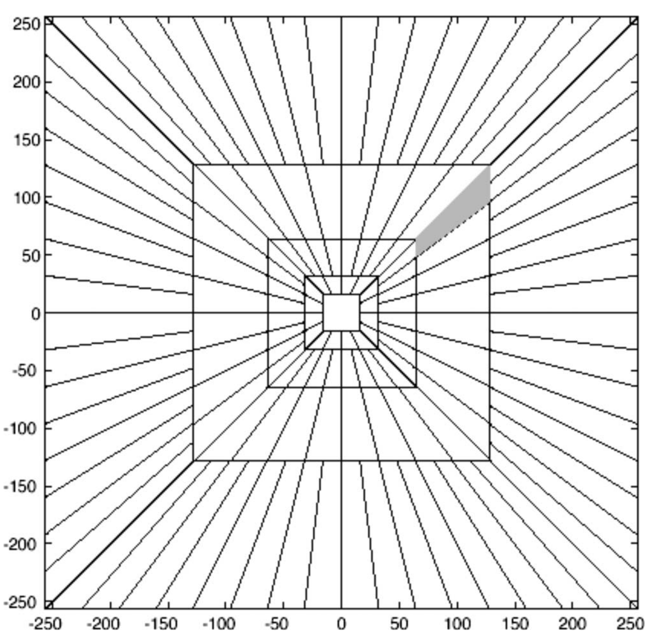

FIG. 3. Discrete curvelet tiling with parabolic pseudopolar support in the frequency plane.

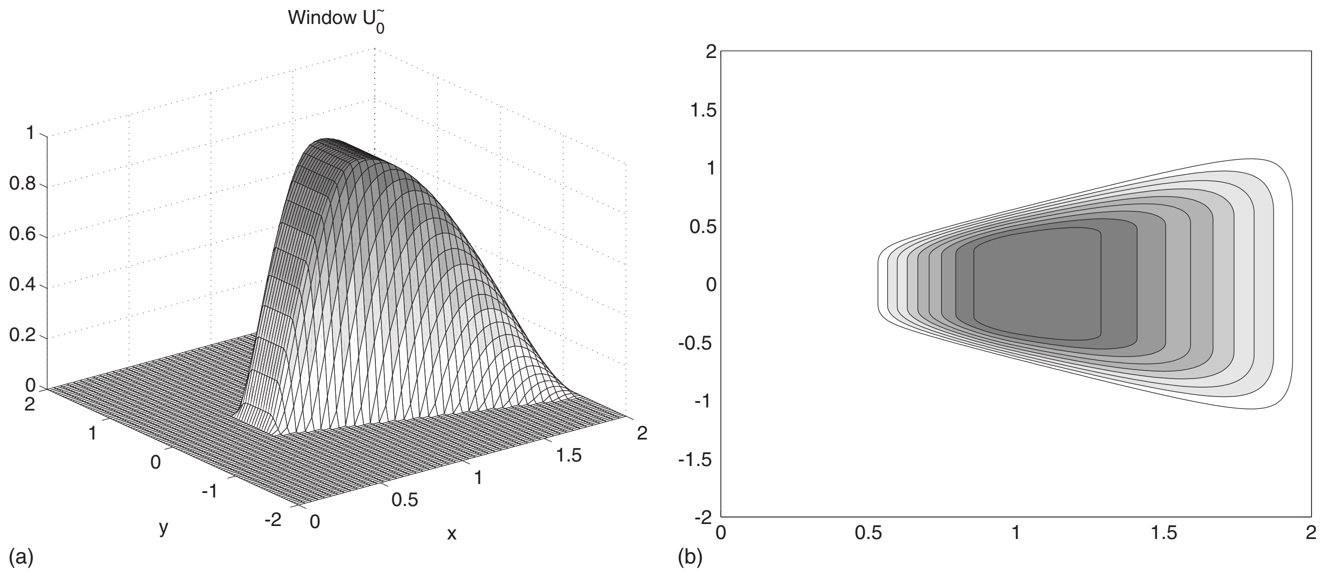

FIG. 4. Window $\tilde{U}_0(\boldsymbol{\xi})$ (left) and its support (right).

$$\{(\xi_1,\xi_2):2^j \le \xi_1 \le 2^{j+1}, -2^{\lfloor j/2\rfloor} \le \xi_2/\xi_1 \le 2^{\lfloor j/2\rfloor}\}.$$

An example of $\tilde{U}_0$ is given in Fig. 4. Let $\tan\,\theta_{j,l} := l2^{-\lfloor j/2\rfloor}$, $l=-2^{\lfloor j/2\rfloor},\ldots,2^{\lfloor j/2\rfloor}-1$ be the set of equispaced slopes and let

$$\tilde{\varphi}_{\boldsymbol{\mu}}(\boldsymbol{x}) = \tilde{\varphi}_{j,l,k}(\boldsymbol{x}) := \tilde{\varphi}_j[S^T_{\theta_{j,l}}(\boldsymbol{x} - \tilde{\boldsymbol{x}}^{(j,l)}_k)],\;\; \boldsymbol{x} = (x_1,x_2) \in \mathbb{R}^2,$$

$$\hat{\tilde{\varphi}}_j(\boldsymbol{\xi}) := \tilde{U}_j(\boldsymbol{\xi}),$$

be the Cartesian counterpart of $\varphi_{j,l,k}$, where $\tilde{\boldsymbol{x}}^{(j,l)}_k := S^{-T}_{\theta_{j,l}}(k_1 2^{-j}, k_2 2^{-\lfloor j/2\rfloor}) =: S^{-T}_{\theta_{j,l}} k_j$, and with the shear matrix

$$S_\theta = \begin{pmatrix} 1 & 0 \\ -\tan\,\theta & 1 \end{pmatrix}.$$

Observe that the angles $\theta_{j,l}$, which range between $-\pi/4$ and $\pi/4$, are not equispaced here, while the slopes are. The set of curvelets $\tilde{\varphi}_{\boldsymbol{\mu}}$ needs to be completed by symmetry and by rotation by $\pm\pi/2$ rad in order to obtain the whole family. We find the Cartesian counterpart of the coefficients in Eq. (1) by

$$\tilde{c}_\mu(f) = \langle f,\tilde{\varphi}_\mu\rangle = \int_{\mathbb{R}^2} \hat{f}(\boldsymbol{\xi})\tilde{U}_j(S^{-1}_{\theta_{j,l}}\boldsymbol{\xi})e^{i\langle \tilde{x}^{(j,l)}_k,\boldsymbol{\xi}\rangle}d\boldsymbol{\xi}$$
$$= \int_{\mathbb{R}^2} \hat{f}(S_{\theta_{j,l}}\boldsymbol{\xi})\tilde{U}_j(\boldsymbol{\xi})e^{i\langle k_j,\boldsymbol{\xi}\rangle}d\boldsymbol{\xi}. \quad (2)$$

The forward (see Algorithm 1) and inverse DCuTs have the same computational cost of $\mathcal{O}(N^2 \log N)$ for an $(N\times N)$ image. The redundancy of the curvelet transform is about 2.8 when wavelets are chosen at the finest scale and 7.2 otherwise (see, e.g., Ref. 17).

Algorithm 1. Two-dimensional discrete curvelet transform.

1. Apply 2D FFT to compute the Fourier coefficients $d_m(f)$ of f.
2. For all m with $S^T_{\theta_{j,l}} m \in \text{supp}\,\tilde{U}_j$ compute the product $d_m(f)\tilde{U}_j(2\pi/NS^T_{\theta_{j,l}}m)$.
3. Apply the inverse 2D FFT to obtain the discrete coefficients $\tilde{c}^D_{\boldsymbol{\mu}}(f)$.

IV. 3D CURVELET TRANSFORM

Real turbulence data are always 3D, which necessitates the use of 3D multiscale geometric methods. 3D curvelets have been recently proposed by Ying *et al.*[23] and Candès *et al.*[17] A fast application of the curvelet transform to 3D turbulent flows has been proposed by Ma and Hussaini.[24] In this paper, the TV-synthesis curvelet transform that combines the 3D curvelet transform with TV minimization is presented.

Similar to 2D problems, we also define $V(t)$ and $W(r)$ to be a pair of smooth, non-negative real-valued window functions, which are called the angular window and the radial window, respectively. V is supported on $[-1,1]$ and W on $[\frac{1}{2},2]$. The windows satisfy the admissibility conditions. Without loss of generation, we introduce the low-pass window W_0 for the coarsest scale, which satisfies the condition

$$W_0(r)^2 + \sum_{j>0} W(2^{-j}r)^2 = 1.$$

These conditions are satisfied by taking, for example, the scaled Meyer windows again.[19] For each $j>0$, the radial window $W(2^{-j}r)$ smoothly extracts the frequency content inside the dyadic corona $2^{j-1}\le r \le 2^{j+1}$. The angular windows partition $\mathbb{R}^3$ into trapezoidal regions, obeying frequency

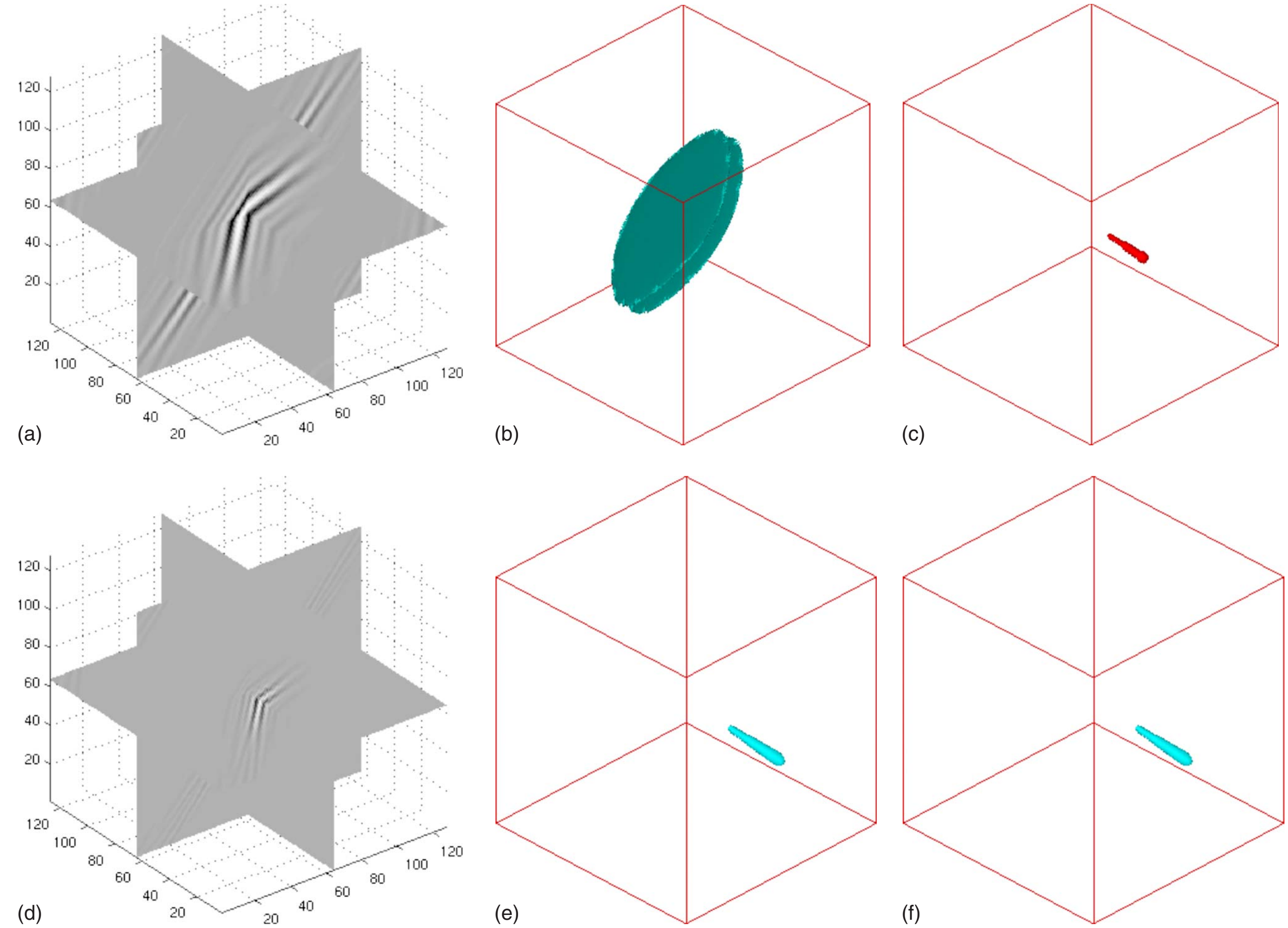

FIG. 5. (Color online) An element of 3D curvelets at a coarse scale (upper row) and fine scale (lower row) is shown in three cross sections (left column) and isosurface (middle column). The right column shows their frequency support. It can be seen that the element with high resolution in the space domain has low resolution in the frequency domain.

parabolic scaling. For $j \geq 0$, define the window $U_j(\boldsymbol{\xi})$, $\boldsymbol{\xi}=(\xi_1,\xi_2,\xi_3) \in \mathbb{R}^3$ in the frequency domain as

$$U_j(\boldsymbol{\xi}) = 2^{-3j/4} W(2^{-j}|\boldsymbol{\xi}|) V(2^{\lfloor j/2 \rfloor}\theta), \quad \boldsymbol{\xi} \in \mathbb{R}^3,$$

where $(|\boldsymbol{\xi}|,\theta)$ denotes the polar coordinates corresponding to $\boldsymbol{\xi}$. The support of U_j is a 3D polar wedge shape, i.e., a half circular cone (refer to Fig. 3 in Ref. 23).

The system of curvelets is now indexed by three parameters (j,l,k), where j denotes scale, l denotes orientation, and $\boldsymbol{k}=(k_1,k_2,k_3)$ denotes spatial location. Define the curvelets as

$$\varphi_{j,l,k}(\boldsymbol{x}) \coloneqq \varphi_j[R_{\theta_{j,l}}(\boldsymbol{x}-\boldsymbol{x}_k^{(j,l)})], \quad \boldsymbol{x}=(x_1,x_2,x_3) \in \mathbb{R}^3,$$

where $\hat{\varphi}_j(\boldsymbol{\xi}) \coloneqq U_j(\boldsymbol{\xi})$, i.e., U_j is the Fourier transform of φ_j, $R_{\theta_{j,l}}$ denotes the rotation matrix with angle $\theta_{j,l}$. Figure 5 shows the elements of 3D curvelets. Observe that in the spatial domain, $\varphi_{j,l,k}$ is of platelike shape, which rapidly decays away from a 2^{-j} by $2^{-j/2}$ cross-sectional rectangle with center $\boldsymbol{x}_k^{(j,l)}$ and orientation $\theta_{j,l}$ with respect to the vertical axis in $\boldsymbol{x}$. The element is smooth within the plate but exhibits oscillating decay in the normal direction to the plate. It obeys a parabolic scaling law between the thickness and the length (thickness $\approx$ length^2) and directional sensitivity (orientations $=1/\sqrt{\text{scale}}$). Figure 5 (right column) shows their support in frequency domain, i.e., the support of 3D frequency window U_j (Fourier transform of the plate-shape elements $\varphi_{j,l,k}$). Similar to the 2D case shown in Figs. 3 and 4, the 3D frequency window U_j is supported by a 3D trapezoid in 3D polar corona grids, where its thickness and length obeys a parabolic scaling law. The directional space-frequency localization of curvelets can be seen clear in Fig. 5. A curvelet element at coarse scale (upper row) has low-frequency content, i.e., the frequency support in Fig. 5(c) close to the center of cube (center point denotes zero frequency), whereas at fine scale (lower row), the elements have high-frequency content, i.e., its frequency support in Fig. 5(f) is away from the center. The fine scale is better in capturing the high-frequency components. Besides the multiscale properties, the anisotropic properties are also obvious from their directional support in the space and frequency domains.

Let $\boldsymbol{\mu}=(j,l,k)$ be the collection of the triple index again. The curvelet coefficients are given by

$$c_{\boldsymbol{\mu}}(f) := \langle f, \varphi_{\boldsymbol{\mu}} \rangle = \int_{\mathbb{R}^3} \hat{f}(\boldsymbol{\xi}) \overline{\hat{\varphi}_{\boldsymbol{\mu}}(\boldsymbol{\xi})} d\boldsymbol{\xi}$$

$$= \int_{\mathbb{R}^3} \hat{f}(\boldsymbol{\xi}) \overline{U_j(R_{\theta_{j,l}} \boldsymbol{\xi})} e^{i\langle x_k^{(j,l)}, \boldsymbol{\xi} \rangle} d\boldsymbol{\xi}. \tag{3}$$

In order to have Cartesian coronas, which is based on concentric cubes instead of spheres, Candès and co-workers[17,23] applied a pseudopolar grid by a modified window of the form

$$\tilde{W}_0(\boldsymbol{\xi}) = \Phi_0(\boldsymbol{\xi}), \quad \tilde{W}_j(\boldsymbol{\xi}) = \sqrt{\Phi_{j+1}^2(\boldsymbol{\xi}) - \Phi_j^2(\boldsymbol{\xi})}, \quad j > 0,$$

where $\Phi_j(\xi_1, \xi_2, \xi_3) = \phi(2^{-j}\xi_1)\phi(2^{-j}\xi_2)\phi(2^{-j}\xi_3)$, and the 1D window ϕ satisfies $0 \le \phi \le 1$, supp $\phi \subset [-2,2]$, and $\phi(r)=1$ for $r \in [-1/2, 1/2]$. As before, ϕ can be taken to be a scaled Meyer window. Redefine the angular window for the lth wedge

$$\tilde{V}_{j,l}(\boldsymbol{\xi}) = V\left(2^{j/2} \frac{\xi_2 - \alpha_l \cdot \xi_1}{\xi_1}\right) V\left(2^{j/2} \frac{\xi_3 - \beta_l \cdot \xi_1}{\xi_1}\right).$$

Here $(1, \alpha_l, \beta_l)$ is the direction of the centerline of the wedge. Every Cartesian corona has six components. The windows in the other five components have similar definitions.

Now we define the modified frequency window $\tilde{U}$ as

$$\tilde{U}_{0,0}(\boldsymbol{\xi}) = \tilde{W}_0(\boldsymbol{\xi}), \quad j = 0,$$

$$\tilde{U}_{j,l}(\boldsymbol{\xi}) = \tilde{W}_j(\boldsymbol{\xi}) \tilde{V}_{j,l}(\boldsymbol{\xi}), \quad 0 < j < j_f,$$

and at the finest scale j_f, the waveletlike isotropic element is defined by the frequency window $\tilde{U}_{j_f,0}(\boldsymbol{\xi}) = \tilde{W}_{j_f}(\boldsymbol{\xi})$. It is clear that $\tilde{U}_{j,l}$ $(0 < j < j_f)$ isolates frequencies near the wedge

$$(\xi_1, \xi_2, \xi_3): 2^{j-1} \le \xi_1 \le 2^{j+1}, \quad -2^{-j/2} \le \xi_2/\xi_1 - \alpha_l \le 2^{-j/2},$$

$$-2^{-j/2} \le \xi_3/\xi_1 - \beta_l \le 2^{-j/2}.$$

Assuming that $L_{p,j,l}(p=1,2,3)$ are three positive integers satisfying Eq. (1), one cannot find $\boldsymbol{\xi}$ and $\boldsymbol{\xi}'$ such that $\boldsymbol{\xi}_p - \boldsymbol{\xi}'_p$ are multiples of $L_{p,j,l}$; and in Eq. (2) the volume $\Lambda_{j,l} = L_{1,j,l} \cdot L_{2,j,l} \cdot L_{3,j,l}$ is minimal. The two conditions guarantee that the data do not overlap with itself during the wrapping process below. Obviously, $\tilde{U}_{j,l}$ is supported now in a 3D rectangular box of integer size $L_{1,j,l} \times L_{2,j,l} \times L_{3,j,l}$.

The discrete curvelets are given by their Fourier formation

$$\hat{\varphi}^D_{\mu}(\boldsymbol{\xi}) = \tilde{U}_{j,l}(\boldsymbol{\xi}) \exp\left(-2\pi i \sum_{p=1,2,3} \frac{k_p \boldsymbol{\xi}_p}{L_{p,j,l}}\right) \Big/ \sqrt{\Lambda_{j,l}}$$

for $0 < k_p < L_{p,j,l}$, $p = 1,2,3$.

Analogously, the transform at the coarsest level is defined as

$$\hat{\varphi}^D_{0,0,k}(\boldsymbol{\xi}) = \tilde{U}_{0,0}(\boldsymbol{\xi}) \exp\left(-2\pi i \sum_{p=1,2,3} \frac{k_p \boldsymbol{\xi}_p}{L_{p,0}}\right) \Big/ \sqrt{\Lambda_0},$$

and a similar formula can be obtained at the finest scale by replacing the scale 0 with j_f and making $L_{p,j_f} = n$.

Now we can find the Cartesian counterpart of the coefficients in Eq. (3) by

$$\tilde{c}^D_{\boldsymbol{\mu}}(f) = \langle f, \varphi^D_{\boldsymbol{\mu}} \rangle = \int_{\mathbb{R}^3} \mathcal{W}(\tilde{U}_{j,l}(\boldsymbol{\xi}) \hat{f}(\boldsymbol{\xi})) e^{i\langle k_j, \boldsymbol{\xi} \rangle} d\boldsymbol{\xi}. \tag{4}$$

The details of 3D DCuT are given in Algorithm 2. The computational complexity of the DCuT is $O(n^3 \log n)$ flops for $n \times n \times n$ data.[17]

Algorithm 2. Three-dimensional discrete curvelet transform.

1. Apply the 3D FFT and obtain Fourier samples $\hat{f}(\boldsymbol{\xi})$, $-n/2 \le \boldsymbol{\xi} < n/2$, $\boldsymbol{\xi} = (\xi_1, \xi_2, \xi_3)$.
2. Multiply the frequency window $\tilde{U}_{j,l}(\boldsymbol{\xi}) \hat{f}(\boldsymbol{\xi})$ for each scale j and angle l.
3. Wrap around the origin and obtain $\mathcal{W}(\tilde{U}_{j,l} \hat{f})(\boldsymbol{\xi})$, where the range for $\boldsymbol{\xi}_p$ is $-L_{p,j,l}/2 \le \boldsymbol{\xi}_p < L_{1,j,l}/2$, $j = (0, j_f)$. No wrapping at scales 0 and j_f.
4. Apply 3D inverse FFT to each $\mathcal{W}(\tilde{U}_{j,l} \hat{f})$ to obtain the discrete coefficients c^D_{μ}.

V. CURVELET SHRINKAGE FOR TURBULENCE

The characterization of turbulent flow structures still remains an open question mostly because our present conceptual and technical tools are inadequate. As discussed in Ref. 43, Hamiltonian mechanics describes equilibrium states of conservative systems, but turbulent flows are nonstationary and dissipative. Classical dynamics only solves systems with a few degrees of freedom, while turbulent flows have a very large, perhaps even infinite number of degrees of freedom. The main factor limiting our understanding of turbulent flows is that we have not yet unambiguously identified the structures responsible for their chaotic and unpredictable behavior. Despite the fact that everyone agrees that coherent vortices are elementary objects in the analysis and simulation of turbulence, there is no universal definition of the coherent structures that everyone agrees on.[7,44,45]

On the other hand, the eddy capturing approaches, such as LES, CVS, and SCALES, are formally derived by applying a filter or nonlinear projection operator to the Navier–Stokes equations. The resulting equations have the same formulation as the original equations but with additional terms, named SGS stresses. The success of the eddy capturing approaches clearly depends on the ability of the SGS model to capture the energy and enstrophy transfer mechanism between resolved and unresolved motions. However the definitions/separations of unresolved SGS and resolved coherent scale are strongly related to the applied filter shape.[46–49] In this paper we will demonstrate that in addition to wavelet denoising, curvelets are an appropriate tool for identifying and separating coherent structures while preserving the geometric information of turbulent flows.

Curvelet shrinkage can be formulated as

$$u_c = \sum_{\boldsymbol{\mu}} \tau[\tilde{c}^D_{\boldsymbol{\mu}}(f)] \varphi_{\boldsymbol{\mu}}, \tag{5}$$

in which $\tau(x)$ could be a hard thresholding,

$$\tau(x) := \begin{cases} x, & |x| \geq \sigma \\ 0, & |x| < \sigma. \end{cases}$$

Applying the method to the vorticity field $\boldsymbol{\omega}$, we have

$$\boldsymbol{\omega} = \boldsymbol{\omega}_c + \boldsymbol{\omega}_I = \sum_{\boldsymbol{\mu}_>} \tilde{c}^D_{\boldsymbol{\mu}_>}(\omega)\varphi_{\boldsymbol{\mu}_>} + \sum_{\boldsymbol{\mu}_<} \tilde{c}^D_{\boldsymbol{\mu}_<}(\omega)\varphi_{\boldsymbol{\mu}_<}. \quad (6)$$

Here $\boldsymbol{\mu}_>$ is an index set for the significant coefficients, whose modulus is larger than or equal to the given threshold value σ, and the index $\boldsymbol{\mu}_<$ stands for the removed insignificant coefficients whose moduli are smaller than σ. This decomposition splits the total vorticity into the resolved coherent field, e.g., $\boldsymbol{\omega}_c(\boldsymbol{x})$ and the residual incoherent field $\boldsymbol{\omega}_I(\boldsymbol{x})$ regardless of the dimensionality of the field. Note that the corresponding coherent velocity $\boldsymbol{V}_c$ and incoherent velocity $\boldsymbol{V}_I$ constitute $\boldsymbol{V}=\nabla\times(\nabla^{-2}\boldsymbol{\omega})$. Therefore, the coherent-incoherent decomposition can be summarized in the following three steps:

(1) Perform DCuT decomposition to obtain the coefficients $\tilde{c}^D_{\mu}$.
(2) Threshold the curvelet coefficients $\tilde{c}^D_{\mu}$ by a given threshold value and rule to separate the significant coefficients and insignificant coefficients.
(3) Reconstruct the thresholded curvelet coefficients using inverse DCuT to obtain the separation fields.

One of the key issues for coherent vortex extraction (e.g., CVS) is how to identify the optimal thresholding value σ. One way is to set the threshold value σ to the variance of the incoherent field, which would result in an iterative procedure.[50] This idea is motivated by Donoho and Johnstone's *VisuShrink* method[51] in denoising, i.e., using the universal threshold $\sigma=\sigma_n\sqrt{2\log M}$, which results in an estimated asymptotically optimal solution in the minimax sense (minimizing the maximum error over all possible M-sample signals). This criterion is based on the *a priori* assumption that the separated incoherent field is a Gaussian white noise component. Analogous to wavelet-based coherent field extraction, the curvelet method uses empirical scale/direction-dependent threshold values[17] $\sigma_{j,l}=\kappa\sigma_n\|\tilde{c}_{j,l}\|_2/N$, where κ is a constant, $N=N_1N_2$ denotes a product of size of subband $\tilde{c}_{j,l}$ in two dimensions and σ_n is the estimated variance of the noise or incoherent random field. Furthermore, the TV-minimization shrinkage addressed in the section below is proposed to eliminate the artifacts arising from conventional hard thresholding. Selection of an optimal threshold for the curvelet-based coherent field extraction is still an open issue.

VI. TV-SYNTHESIS CURVELET SHRINKAGE

Tools from computational harmonic analysis suffer from the famous pseudo-Gibbs phenomena, i.e., oscillation artifacts near the discontinuities, although curvelets have much improved the problem in comparison with traditional wavelets. Following the previous work,[20,32,52,53] a TV minimization is combined with the synthesis of curvelet shrinkage to reduce the pseudo-Gibbs and elementlike artifacts in extracted fields. Another motivation to use the TV is that TV-based curvelet shrinkage is an ease of extracting incoherent fields when applying the method to CVS or SCALES of turbulence.

For a function $\boldsymbol{u}$ with $|\nabla\boldsymbol{u}|\in L^1(\Omega)$, the TV functional is defined[54] as

$$\mathrm{TV}(\boldsymbol{u}) = \int_\Omega |\nabla\boldsymbol{u}(x)|d\boldsymbol{x}.$$

To circumvent computational difficulties arising from the nondifferentiation of the modulus at zero, the TV functional is often replaced by

$$\mathrm{TV}(\boldsymbol{u}) = \int_\Omega \sqrt{|\nabla\boldsymbol{u}(x)|^2+\beta^2}d\boldsymbol{x},$$

with a small parameter $\beta>0$. In the following description, we mainly restrict our attention to the 3D problem. For the 2D problem, we refer readers to Refs. 20 and 32, where the authors combined TV minimization with the ridgelet and curvelet transform for image processing. The discrete version of the TV functional for $\boldsymbol{u}:=(u_{\iota,\kappa,\nu})_{(\iota,\kappa,\nu)\in I_n^3}$ is given by

$$\mathrm{TV}(\boldsymbol{u}) = \sum_{\iota,\kappa,\nu}\sqrt{|(\delta_1\boldsymbol{u})_{\iota,\kappa,\nu}|^2+|(\delta_2\boldsymbol{u})_{\iota,\kappa,\nu}|^2+|(\delta_3 u)_{\iota,\kappa,\nu}|^2+\beta^2}d\boldsymbol{x},$$

where $(\delta_1 u)_{\iota,\kappa,\nu}=u_{\iota+1,\kappa,\nu}-u_{\iota,\kappa,\nu}$, $(\delta_2 u)_{\iota,\kappa,\nu}=u_{\iota,\kappa+1,\nu}-u_{\iota,\kappa,\nu}$, and $(\delta_3 u)_{\iota,\kappa,\nu}=u_{\iota,\kappa,\nu+1}-u_{\iota,\kappa,\nu}$. More precisely, for a given $\boldsymbol{u}$ let

$$\mathbb{U} := \{u := (u_{\iota,\kappa,\nu})_{(\iota,\kappa,\nu)\in I_n^3} : c^D_{\boldsymbol{\mu}>} = c^D_{\boldsymbol{\mu}},\ \forall\ \boldsymbol{\mu}\in\Lambda\}.$$

Then we are looking for the solution of the constrained minimization problem

$$\min_{\boldsymbol{u}\in\mathbb{U}} \mathrm{TV}(\boldsymbol{u}).$$

If the linear subspace $\mathbb{V}$ consists of functions on I_n^3 given by

$$\mathbb{V} := \{\boldsymbol{v} := (v_{\iota,\kappa,\nu})_{(\iota,\kappa,\nu)\in I_n^3} : c^D_{\boldsymbol{\mu}} = 0,\ \forall\ \boldsymbol{\mu}\in\Lambda\},$$

the idea of TV minimization is to remove the pseudo-Gibbs oscillations by minimizing the functional

$$F(\boldsymbol{u}) = \int_\Omega |\boldsymbol{u}-\boldsymbol{u}_0|^2 d\boldsymbol{x} + \lambda\mathrm{TV}(\boldsymbol{u}) \quad (7)$$

for $\boldsymbol{u}\in\{\boldsymbol{u}_c+\boldsymbol{v},\boldsymbol{v}\in\mathbb{V}\}$, where $\boldsymbol{u}_0$ is an original flow, $\boldsymbol{u}_c$ is a reconstructed flow after curvelet hard thresholding, and $\mathbb{V}$ is a linear subspace of functions consisting of the components removed by thresholding. It should be noted that because of the constraint on the subspace $\mathbb{V}$, Eq. (7) is not the usual Rudin–Osher–Fatemi TV model as in Ref. 54 but instead is a variant of the TV problem, which was originally inspired by Durand *et al.*[52] for wavelets and extended by Ma *et al.*[20,32,53]

Using $\boldsymbol{u}_c$ as an initial guess, the constrained TV minimization can be computed by a projected subgradient descent scheme[52]

$$\boldsymbol{u}^{l+1} = \boldsymbol{u}^l - t_l P_V[g_{\mathrm{TV}}(\boldsymbol{u}^l)]. \quad (8)$$

Here $g_{\mathrm{TV}}(\boldsymbol{u})$ denotes the subgradient of TV at $\boldsymbol{u}$. The step size t_l can be taken appropriately to ensure convergence. $P_V(\boldsymbol{u})$ denotes a projection of $\boldsymbol{u}$ on the constrained subspace $\mathbb{V}$. This means that only the coefficients with absolute value

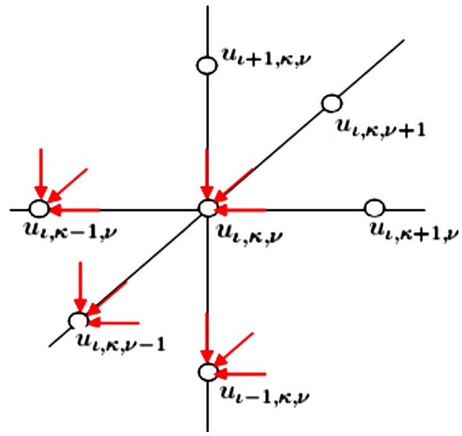

FIG. 6. (Color online) Diagram of 3D coordinate grid for computation of $\nabla_u \mathrm{TV}(u)$. The four points with arrows are points related to the derivation of the sum with respect to $\boldsymbol{u}_{\iota,\kappa,\nu}$. The arrow head indicates the Euler forward difference scheme.

smaller than a given threshold σ will be changed by the minimization process. Let T be the curvelet transform and T^{-1} be its inverse, then we have $P_V(\boldsymbol{u})=T^{-1}\tau^{-1}T(\boldsymbol{u})$ where τ^{-1} denotes the so-called inverse thresholding function,

$$\tau^{-1}(\boldsymbol{x}) := \begin{cases} 0, & |\boldsymbol{x}| \ge \sigma, \\ \boldsymbol{x}, & |\boldsymbol{x}| < \sigma. \end{cases}$$

A crucial step is to compute the gradient of TV, i.e., $g_{\mathrm{TV}}(\boldsymbol{u})$ or $\nabla_u \mathrm{TV}(\boldsymbol{u})$. For 2D problems, we have[32]

$$\begin{aligned}\nabla_u \mathrm{TV}(\boldsymbol{u}) := {} & (2\boldsymbol{u}_{\iota,\kappa} - \boldsymbol{u}_{\iota,\kappa+1} - \boldsymbol{u}_{\iota+1,\kappa}) \\ & \times[(\boldsymbol{u}_{\iota,\kappa+1} - \boldsymbol{u}_{\iota,\kappa})^2 + (\boldsymbol{u}_{\iota+1,\kappa} - \boldsymbol{u}_{\iota,\kappa})^2 + \beta^2]^{-1/2} \\ & + (\boldsymbol{u}_{\iota,\kappa} - \boldsymbol{u}_{\iota-1,\kappa})[(\boldsymbol{u}_{\iota-1,\kappa+1} - \boldsymbol{u}_{\iota-1,\kappa})^2 \\ & + (\boldsymbol{u}_{\iota-1,\kappa} - \boldsymbol{u}_{\iota,\kappa})^2 + \beta^2]^{-1/2} + (\boldsymbol{u}_{\iota,\kappa} - \boldsymbol{u}_{\iota,\kappa-1}) \\ & \times[(\boldsymbol{u}_{\iota+1,\kappa-1} - \boldsymbol{u}_{\iota,\kappa-1})^2 \\ & + (\boldsymbol{u}_{\iota,\kappa} - \boldsymbol{u}_{\iota,\kappa-1})^2 + \beta^2]^{-1/2} \end{aligned} \quad (9)$$

for the inner points $(\iota,\kappa) \in I_n^2$ and corresponding modification at the boundary ∂I_n^2.

For 3D problems, there is a little complex representation. Figure 6 illustrates the 3D grids for computation of $\nabla_u \mathrm{TV}(\boldsymbol{u})$. The four points denoted by red arrows are points that are related to the derivation of the sum with respect to $\boldsymbol{u}_{\iota,\kappa,\nu}$. The arrow head indicates the direction of the Euler forward difference scheme. The derivation of the TV at location $\boldsymbol{u}_{\iota,\kappa,\nu}$ is given by

$$\begin{aligned}\nabla_u \mathrm{TV}(u) := {} & (3\boldsymbol{u}_{\iota,\kappa,\nu} - \boldsymbol{u}_{\iota+1,\kappa,\nu} - \boldsymbol{u}_{\iota,\kappa,\nu+1} - \boldsymbol{u}_{\iota,\kappa+1,\nu})A^{-1/2} \\ & + (\boldsymbol{u}_{\iota,\kappa,\nu} - \boldsymbol{u}_{\iota,\kappa-1,\nu})B^{-1/2} + (\boldsymbol{u}_{\iota,\kappa,\nu} - \boldsymbol{u}_{\iota,\kappa,\nu-1})C^{-1/2} \\ & + (\boldsymbol{u}_{\iota,\kappa,\nu} - \boldsymbol{u}_{\iota-1,\kappa,\nu})D^{-1/2} \end{aligned} \quad (10)$$

for the inner points $(\iota,\kappa) \in I_n^3$ and corresponding modification at the boundary ∂I_n^3. Here

$$A = (\boldsymbol{u}_{\iota+1,\kappa,\nu} - \boldsymbol{u}_{\iota,\kappa,\nu})^2 + (\boldsymbol{u}_{\iota,\kappa,\nu+1} - \boldsymbol{u}_{\iota,\kappa,\nu})^2 + (\boldsymbol{u}_{\iota,\kappa+1,\nu} - \boldsymbol{u}_{\iota,\kappa,\nu})^2,$$

$$B = (\boldsymbol{u}_{\iota+1,\kappa-1,\nu} - \boldsymbol{u}_{\iota,\kappa-1,\nu})^2 + (\boldsymbol{u}_{\iota,\kappa-1,\nu+1} - \boldsymbol{u}_{\iota,\kappa-1,\nu})^2 + (\boldsymbol{u}_{\iota,\kappa,\nu} - \boldsymbol{u}_{\iota,\kappa-1,\nu})^2,$$

$$C = (\boldsymbol{u}_{\iota+1,\kappa,\nu-1} - \boldsymbol{u}_{\iota,\kappa,\nu-1})^2 + (\boldsymbol{u}_{\iota,\kappa+1,\nu-1} - \boldsymbol{u}_{\iota,\kappa,\nu-1})^2 + (\boldsymbol{u}_{\iota,\kappa,\nu} - \boldsymbol{u}_{\iota,\kappa,\nu-1})^2,$$

$$D = (\boldsymbol{u}_{\iota,\kappa,\nu} - \boldsymbol{u}_{\iota-1,\kappa,\nu})^2 + (\boldsymbol{u}_{\iota-1,\kappa,\nu+1} - \boldsymbol{u}_{\iota-1,\kappa,\nu})^2 + (\boldsymbol{u}_{\iota-1,\kappa+1,\nu} - \boldsymbol{u}_{\iota-1,\kappa,\nu})^2.$$

Essentially, TV minimization does not set the insignificant coefficients to zero as conventional shrinkage does but typically removes optimally small values to eliminate the artifacts.

It should be noted that Schneider *et al.*[50] proposed an iterative wavelet shrinkage to extract coherent vortices out of turbulent flows. Using iterative thresholding, the incoherent background shows a tendency toward enstrophy equipartition, thus one can split each flow realization into coherent vortices and incoherent quasi-Gaussian white noise better than using conventional one-step hard thresholding. The close relationship between wavelet/curvelet shrinkage and nonlinear diffusion has been explored recently (see, e.g., Refs. 19 and 55). A comparison of the performances of our proposed TV-curvelet shrinkage with Schneider's iterative scheme for coherent vortex extraction will be addressed in a forthcoming paper.

VII. EXPERIMENTS

In contrast to LES, where a low-pass filter with grid truncation can be defined either explicitly or implicitly by the numerical method, a coherent/incoherent decomposition of turbulent flow fields should be performed explicitly for each flow realization. In addition, to materialize the full potential of coherent/incoherent decomposition, the number of the coherent modes should be considerably smaller than the number of incoherent modes. It was clearly shown in Refs. 5 and 8 that Fourier filters are not suitable for extraction of coherent vortices mainly because they oversmooth the filtered structures resulting in a non-Gaussian partially coherent residual field. In addition, Fourier low-pass filtering introduces spurious oscillations. Wavelet filters work well for coherent vortex extraction, yet due to the homogenous nature of wavelet decomposition, they do not consider the shape and geometry of the vortices. The proposed curvelet-based filter addresses this deficiency and improves wavelet-based coherent feature extraction characteristics both in terms of sparse representation and edge preserving characteristics.

A. 2D turbulent flows

1. Power spectra analysis of curvelets

The almost perfect representation of both energy and enstrophy spectra by the coherent field is essential to the success of both CVS and SCALES approaches. The good spectra properties of wavelet-based coherent vortex extraction of turbulent fields have been documented by numerous authors (e.g., Refs. 5 and 8). In order to verify the feasibility

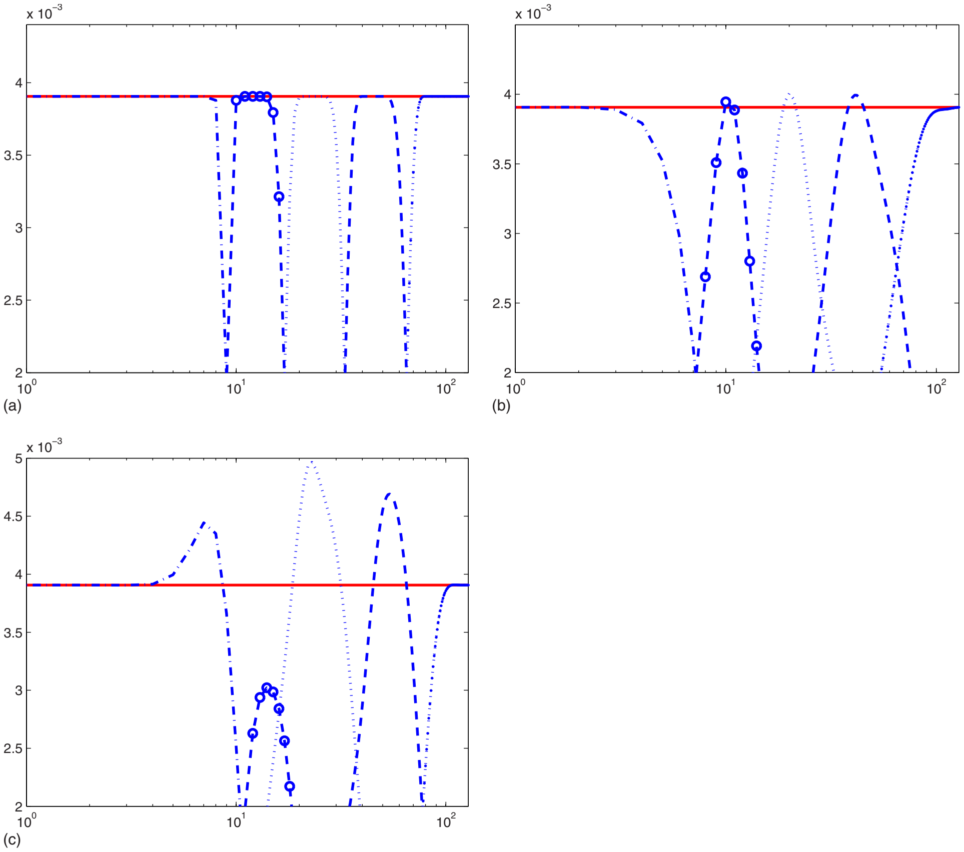

FIG. 7. (Color online) Fourier energy spectra of a unit impulse field at different scales from coarse to fine by (a) curvelet transform, (b) Selesnick's wavelet transform, and (c) Daubechies' DB6 wavelet transform.

of curvelet filters for coherent/incoherent turbulent field decomposition, the spectral properties of curvelet decomposition are compared to wavelet transforms.

In order to highlight the superior spectral properties of curvelet-based decomposition, let us consider a 2D unit impulse, i.e., unity at the center and zeros elsewhere. Figure 7 shows the Fourier energy spectra at different scales using the curvelet transform, Selesnick's wavelet transform,[56] and Daubechies' DB6 wavelet transform,[42] respectively. It should be noted that 1D Fourier spectra are displayed for all tests (the fields have been averaged in another dimension). The solid line denotes the full field, while various broken lines denote individual levels/scales of resolution. The different frequency bands are computed by four steps: (1) decompose the 2D test field into curvelet domain; (2) filter in each subband, i.e., keep coefficients in this scale unchanged and set coefficients as zeros in others scales; (3) inverse transform the filtered subband to the physical domain; and (4) compute the Fourier transform for the reconstructed subbands to get different frequency bands. The Fourier spectra represent a repartition of frequency from the signal. It describes how a signal is distributed along frequency. Daubechies's DB6 wavelet leads to artifacts in frequency decomposition to some extent. In the following experiments, Selesnick's wavelet transform is used as a comparison of the curvelet transform. The curvelets demonstrate their ability to have sharper spectral bounds and have less overlap in the spectral content of neighboring levels of resolution. These indicate that the curvelet transform owns high-resolution frequency partitions, which is useful for the analysis of multiscale structures of turbulence.

2. Sparse partial reconstruction

Compression properties of the curvelet transform in the context of coherent/incoherent turbulent field decomposition are examined next using a vorticity field extracted from 2D DNS. The original field (shown in Fig. 8) is an isotropic decaying turbulence started from the random noise. The Reynolds number of this flow is 4000. Figure 9 shows the high compressive rate of turbulent flows while preserving the geometry in the base of the curvelet transform. The partial

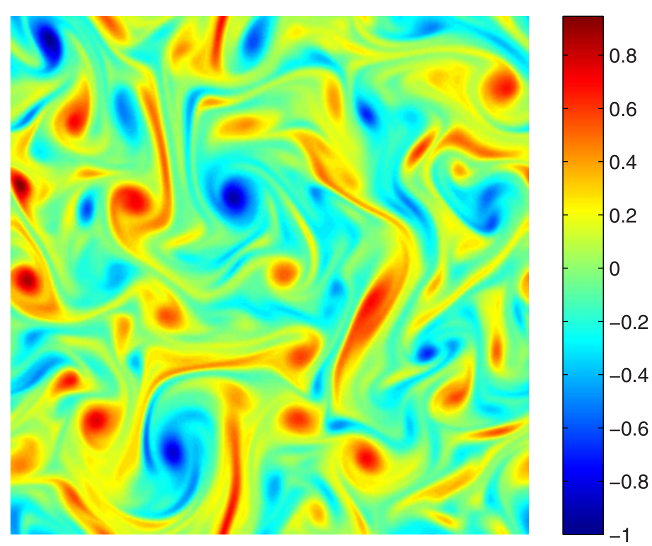

FIG. 8. (Color online) Total vorticity of a turbulence flow on size 512×512 with Reynolds number of 4000.

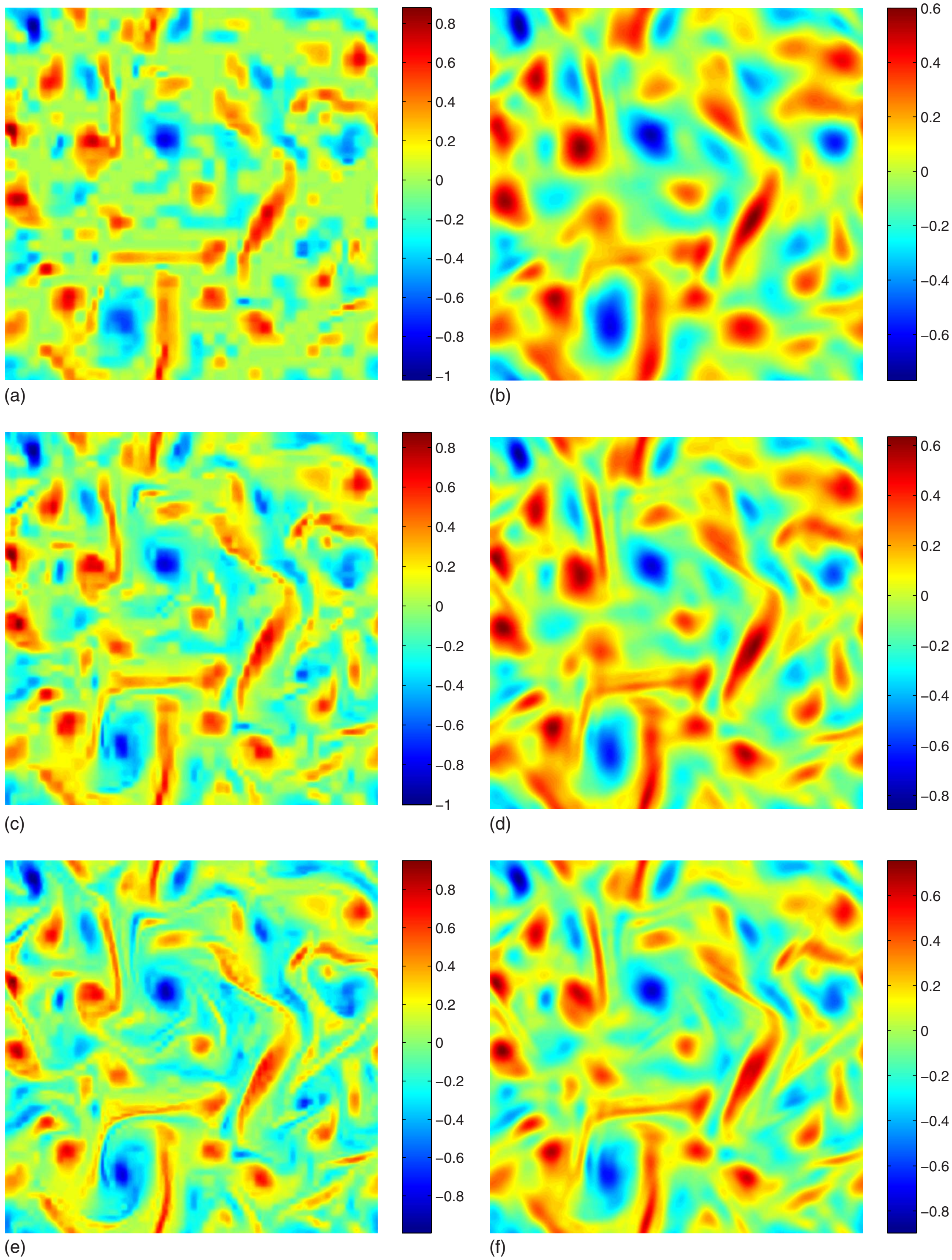

FIG. 9. (Color online) The reconstructed vorticity by wavelets (left) and curvelets (right). The numbers of coefficients from the first row to third row are largest 512, 1024, and 2048.

reconstruction using the wavelet transform (as shown in the left column) and curvelet transform (as shown in the right column) are given. Partially reconstructed results obtained using the largest 512, 1024, and 2048 coefficients are, respectively, shown in the rows from top to bottom. Although the curvelet transform is redundant, the reconstructed results show better edge preservation than wavelets even using the same numbers of coefficients. This is because curvelets are optimally sparse at representing the edges of the vortical structures. Wavelet-based filtered fields display strong oscillations along the edges obviously due to the poor ability of wavelets at representing line singularities. The edges and structures of the vortex are distorted by these artifacts, which could lead to computational errors when the filtering method is applied in the context of both CVS and SCALES. In contrast, curvelet-based decomposition resulted in vortices that

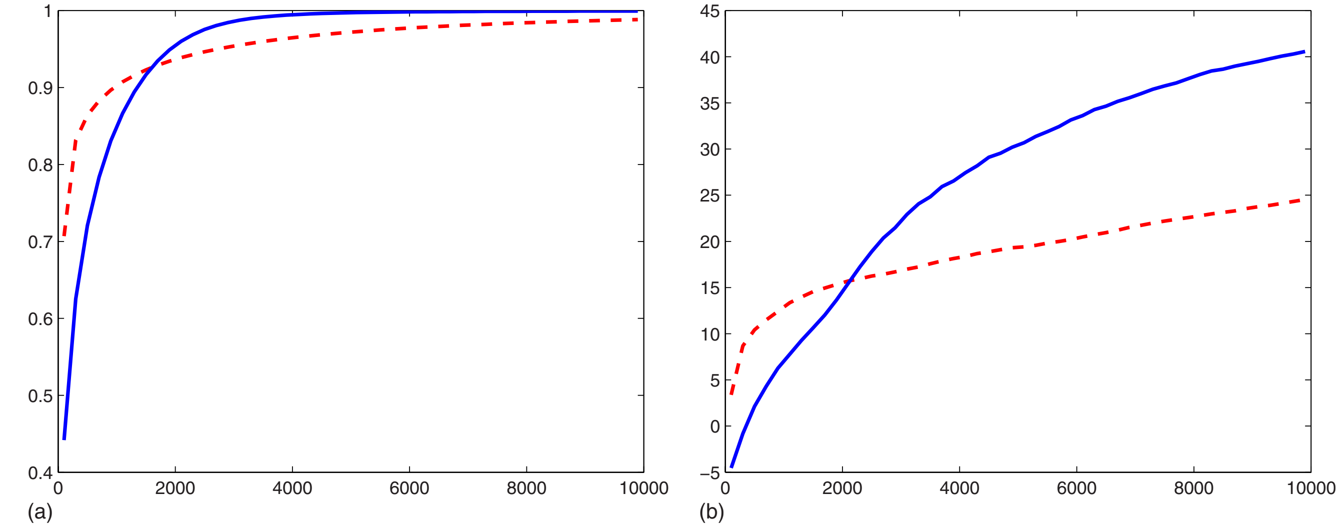

FIG. 10. (Color online) (a) Number of reconstructed coefficients vs rate of reconstructed enstrophy. (b) Number of reconstructed coefficients vs SNR of reconstructed fields. The horizontal coordinate denotes the number of coefficients. The solid line denotes wavelet transform and the dashed line denotes curvelet transform.

are well preserved mostly due to the ability of the curvelet transform to represent edges much more sparsely than by using wavelets.

The superior reconstruction properties of the curvelet transform in comparison to the wavelet transform are demonstrated in Fig. 10, where the percentage of the retained enstrophy and signal-to-noise ratio (SNR) are shown as function of the number of reconstructed coefficients for both wavelets and curvelets. If one uses a small number of coefficients, one can achieve better approximate reconstruction using curvelets. However, after a critical number, the wavelet transform achieves a high value because there are too many insignificant coefficients (close to zero) using the redundant curvelet transform. If one keeps the 1% largest coefficients, the curvelet and wavelet reconstructed vortices retain 99.42% and 97.81% of the total enstrophy of the original flow, respectively. In this case, the SNRs of the reconstructed flows are 31.11 and 19.74 dB by the curvelet and wavelet transforms, respectively. Figure 11 shows the reconstructed enstrophy and SNR versus the ratio of the number of reconstructed coefficients to the number of total coefficients. The difference between Figs. 10 and 11 is the horizontal coordinate. The curvelet transform has better performance at maintaining the main geometric features.

3. Multiscale geometric decomposition and coherent vortex extraction

We first test how geometric structures can be decomposed in multiple scales by the curvelet transform, in comparison with the wavelet transform. Figure 12 shows the comparisons of decomposing the turbulent flow shown in

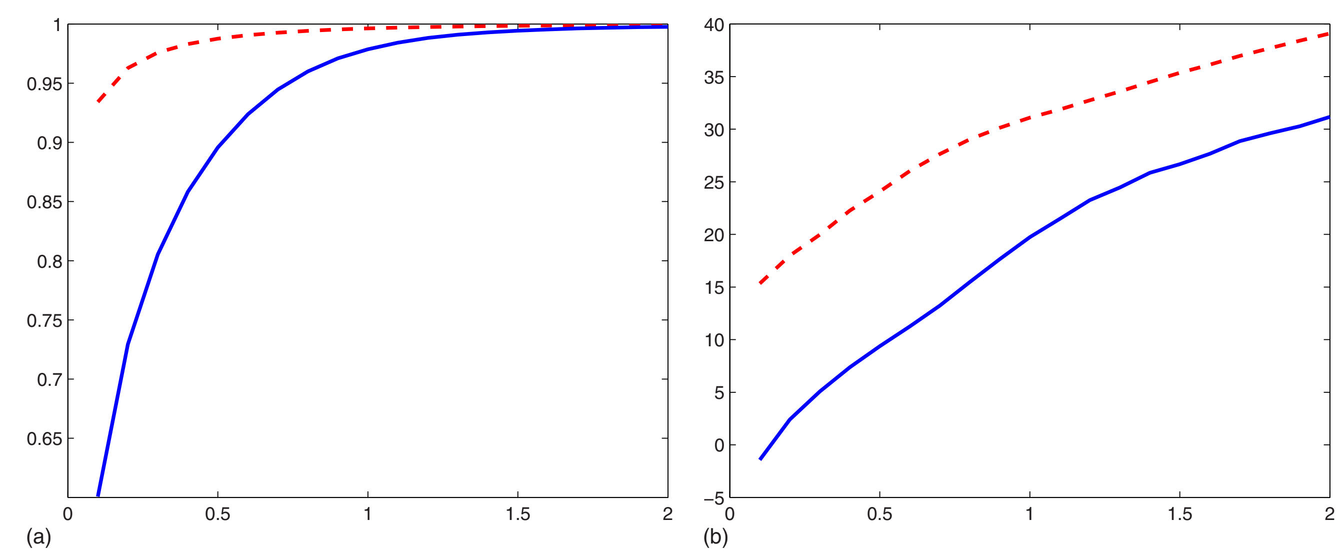

FIG. 11. (Color online) (a) The ratio of reconstructed coefficients vs rate of reconstructed enstrophy. (b) The ratio of reconstructed coefficients vs SNR of reconstructed fields. The horizontal coordinate denotes the percent rate of reconstructed coefficient numbers to total coefficient numbers. The solid line denotes wavelet transform and the dashed line denotes curvelet transform.

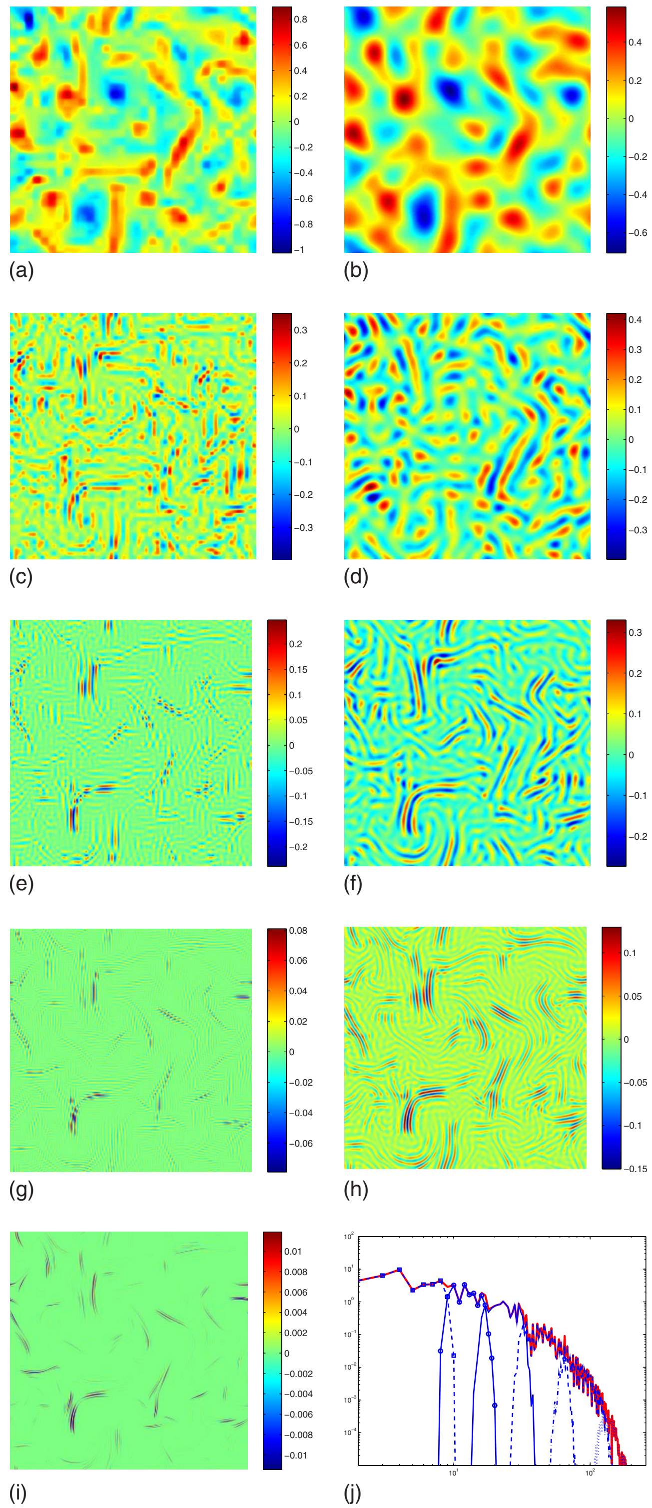

FIG. 12. (Color online) Multiscale geometric decomposition of turbulent flow. (Left column) wavelet decomposition. (Right column) Curvelet decomposition. From top to bottom: coarse scale to fine scale.

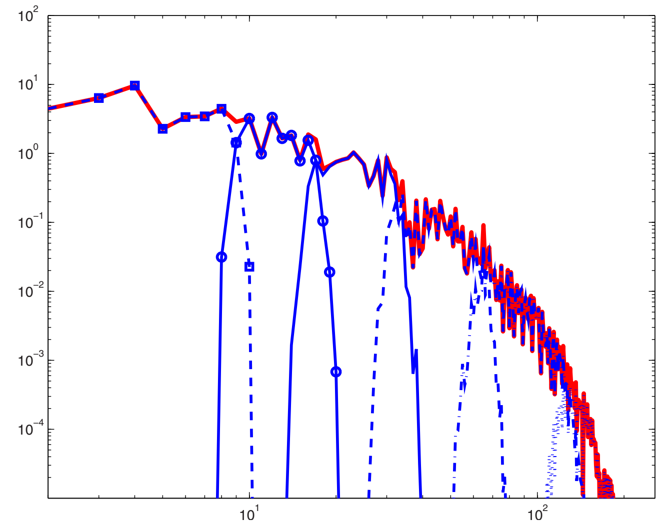

FIG. 13. (Color online) Enstrophy spectra in every scale by curvelet decomposition. The upper solid line denotes the original field. The lines from left to right denote the scale from coarse to fine.

Fig. 8(b). It can be clearly seen that the curvelet transform (shown in the right column) keeps the geometric structures much better than the wavelet transform (shown in the left column). Discontinuous artifacts destroy the structures using wavelet decomposition. Figure 13 displays the enstrophy spectra in every scale by curvelet decomposition. The spectra curves of wavelet decomposition, which we do not show here, display much higher oscillation.

The coherent/incoherent fields can be decomposed using curvelet and wavelet thresholding. Hard thresholding with $\sigma_{j,l}=\kappa\sigma_n\|\tilde{c}_{j,l}\|_2/N$ is used and compared to wavelet-based decomposition. Figures 14(a) and 14(b) are coherent fields extracted by the wavelet transform and the curvelet transform, respectively. Figures 14(c) and 14(d) show their residual fields. The corresponding statistical analyses of the residual fields are given in Figs. 14(e) and 14(f). It can be seen that both residual incoherent fields display near Gaussian distributions. Figure 15 shows the enstrophy spectra of the curvelet's residual field. The solid line denotes the original field, the dot-dashed line denotes the coherent fields, and the dashed line denotes residual fields. For the curvelet transform, the reconstructed coherent field is almost the same as the original fields. Both wavelet and curvelet transforms demonstrate the ability to extract the white noise component for low wavenumbers. Due to the redundancy of the curvelet transform, the curvelet filtered field has a higher power compared to the wavelet filtered one when the same percentage of wavelet/curvelet coefficients is kept. The results highly depend on the choice of the thresholding function and thresholding value. In this paper, experiential threshold values of 0.062 and 0.214 are chosen for curvelet and wavelet hard thresholding, respectively. How to choose optimal thresholding values for decomposition of coherent and residual fields in practice is still an open problem. The current form can be considered a starting point, and there is much room for refinement.

4. Curvelet compression

In order to analyze the effectiveness of curvelet coherent vortex extraction and denoising properties, it is illustrative to consider curvelet compression measured by the compression coefficient defined by $(N-N_{>})/N\times 100\%$, where $N_{>}$ is the number of retained coefficients for a given threshold ϵ. In Fig. 16, the solid and dotted lines denote, respectively, curvelet and wavelet compression. The percentage of the un-

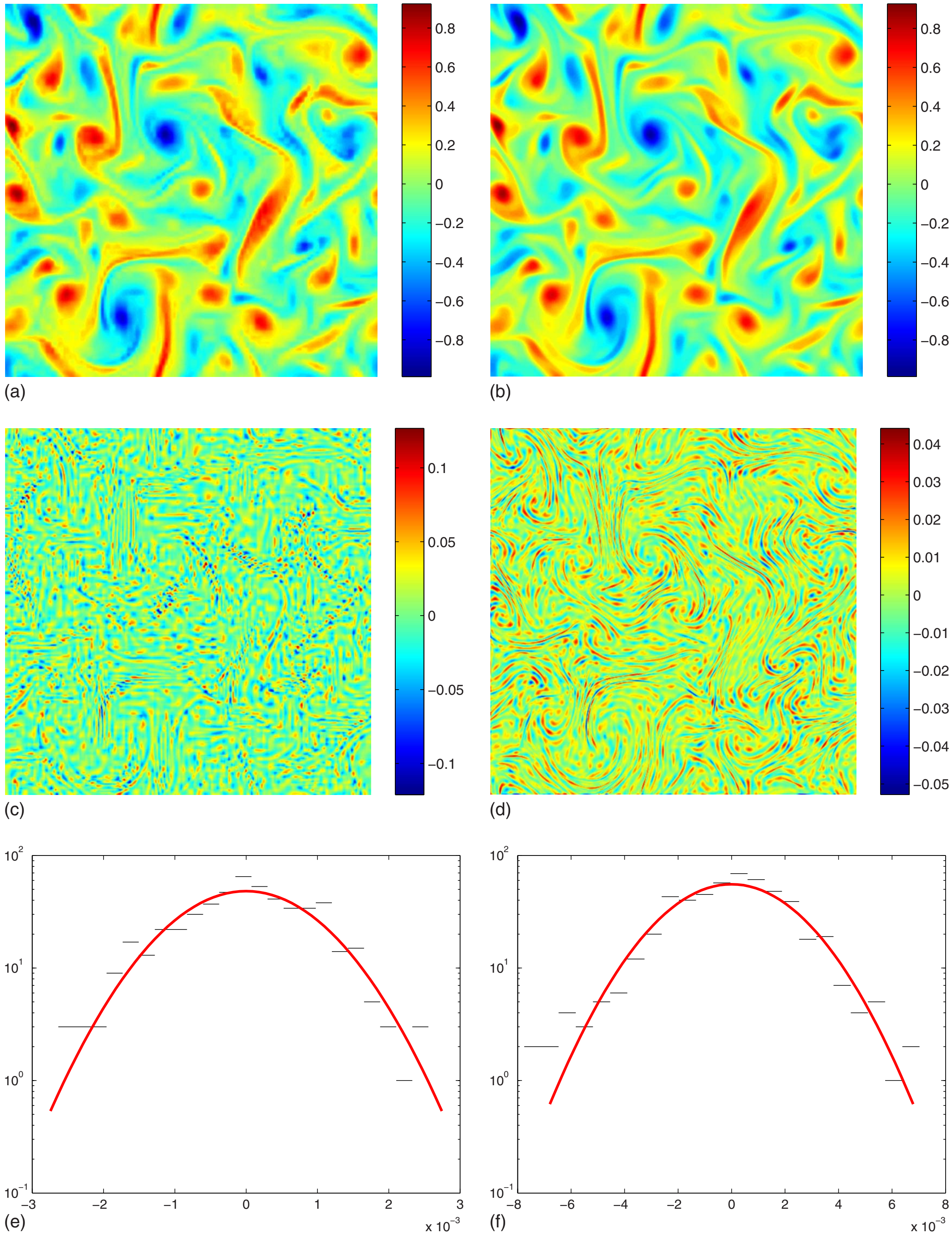

FIG. 14. (Color online) [(a) and (b)] Coherent fields by wavelets (left column) and curvelets (right column). [(c) and (d)] Residual fields. [(e) and (f)] Statistical analysis of the residual fields. The solid line denotes the Gaussian normal distribution in log-linear scale.

resolved energy, i.e., the energy contained in the filtered field, is shown in the same figure by the dashed and dot-dashed lines corresponding to curvelets and wavelets, respectively. Although the curvelet transform is redundant, the number of significant coefficients decreases rapidly with an increase in the threshold value. Quantitatively, using the threshold value of 1.0, we have a compression coefficient and percentage of filtered enstropy of 99.86% and 6.60% for curvelets and 98.44% and 2.74% for wavelets.

5. Denoising of vortex flow

The proposed algorithm is also applicable to the experimental data. An example of such application is given in Fig. 17, where the transient state of the evolution of the vortex issued from the Coriolis platform in Grenoble, France, is shown. Although the added noise is useful as a visual aid, we suppress it in order to extract the vortex for a constraint in data assimilation (see Ref. 18). Figure 17(b) is the extracted

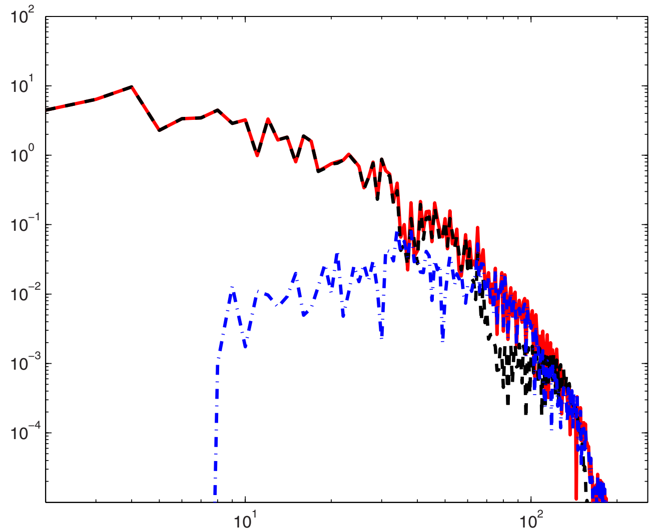

FIG. 15. (Color online) Enstrophy spectra by curvelet transform. The solid line, dot-dashed line, and dashed line denote original flow, coherent field, and residual field, respectively.

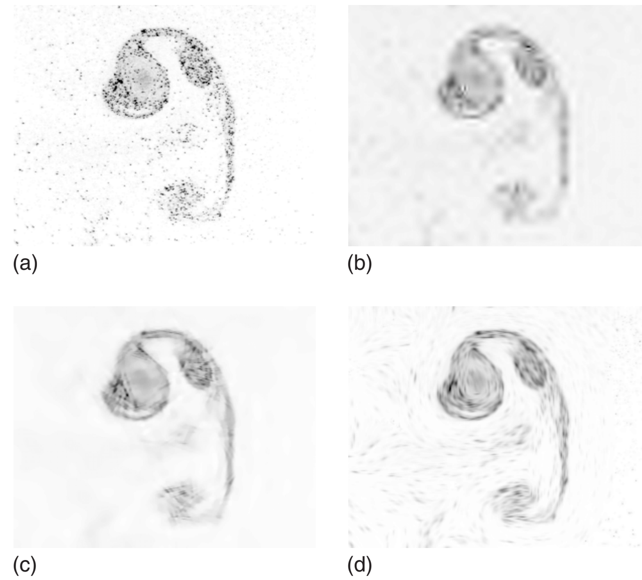

FIG. 17. (Color online) Denoising of a transient vortical flow: (a) original flow, (b) by using wavelets, (c) by the proposed method, and (d) by coherence-enhancing diffusion.

result using the Db4 orthogonal wavelet transform. Figure 17(c) is obtained using the proposed curvelet-based method in Eq. (8) with ten iterations. Figure 17(d) is obtained using Weickert's coherence-enhancing diffusion[41] with coherent parameter of 15, step size of 0.24, and an iteration of 30. The parameters used for each method have been chosen empirically to optimize the visual quality.

B. 3D turbulent flows

In this section, we apply curvelet thresholding for 3D vorticity fields. In order to fully assess the ability of the curvelet transform to extract coherent structures from real 3Dl turbulence fields, we analyze the vorticity field using 3D curvelets and nearly isotropic orthogonal 3D wavelets. In Fig. 18, we show the performance of partial reconstruction by curvelets and wavelets. Here the results are obtained by reconstructing the largest 1% of curvelet coefficients and wavelet coefficients in different visualization contexts (i.e., different rows are the same result shown by different display approaches in order to see the edges and structures more clearly). The left column shows the original turbulent flow with size of 64^3, taken from the data of 256^3 DNSs of decaying compressible, isotropic turbulence at fluctuation Mach number of $M=0.488$ and at Taylor Reynolds number of $\mathrm{Re}_{\lambda}=l75$ (case D9 of Ref. 57). The middle and right columns are the results of the 3D curvelet and wavelet shrinkage, respectively. The figures in each row, from top to bottom, are 3D cross sections, contour plots, and isosurface plots, respectively. It is clear that the reconstructed coherent

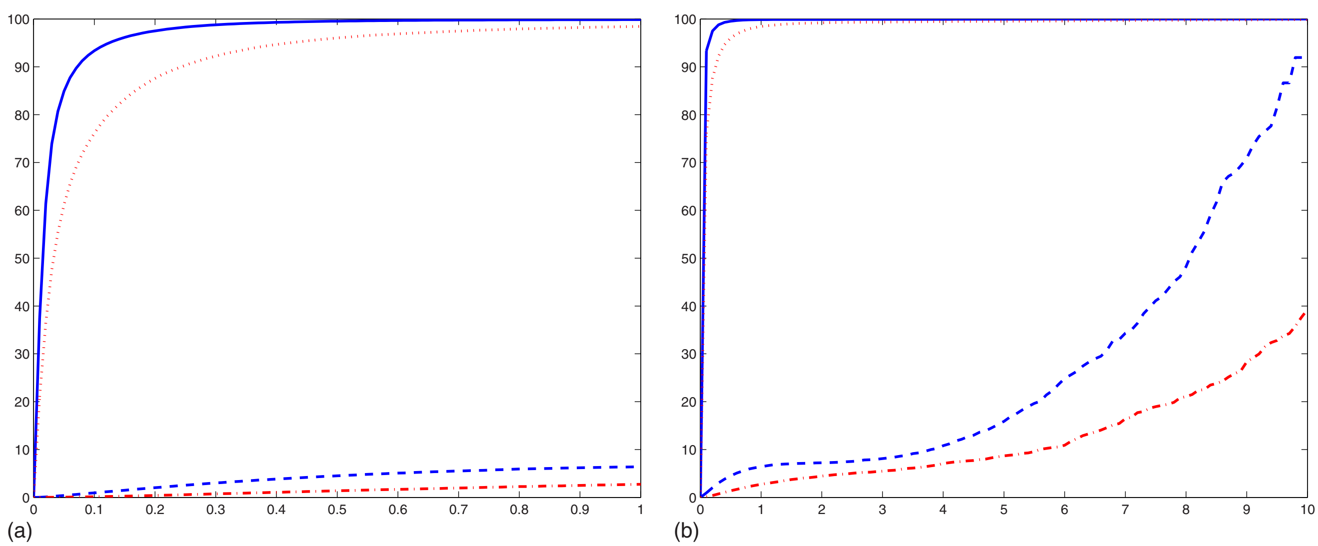

FIG. 16. (Color online) The compression ratio of the coefficients and the percentage of the enstrophy of retained coefficients as a function of the threshold value. (a) Small threshold values varying from 0 to 1. (b) Large threshold values varying from 0 to 10. The vertical coordinates denote compression ratios and the horizontal coordinate denotes threshold value.

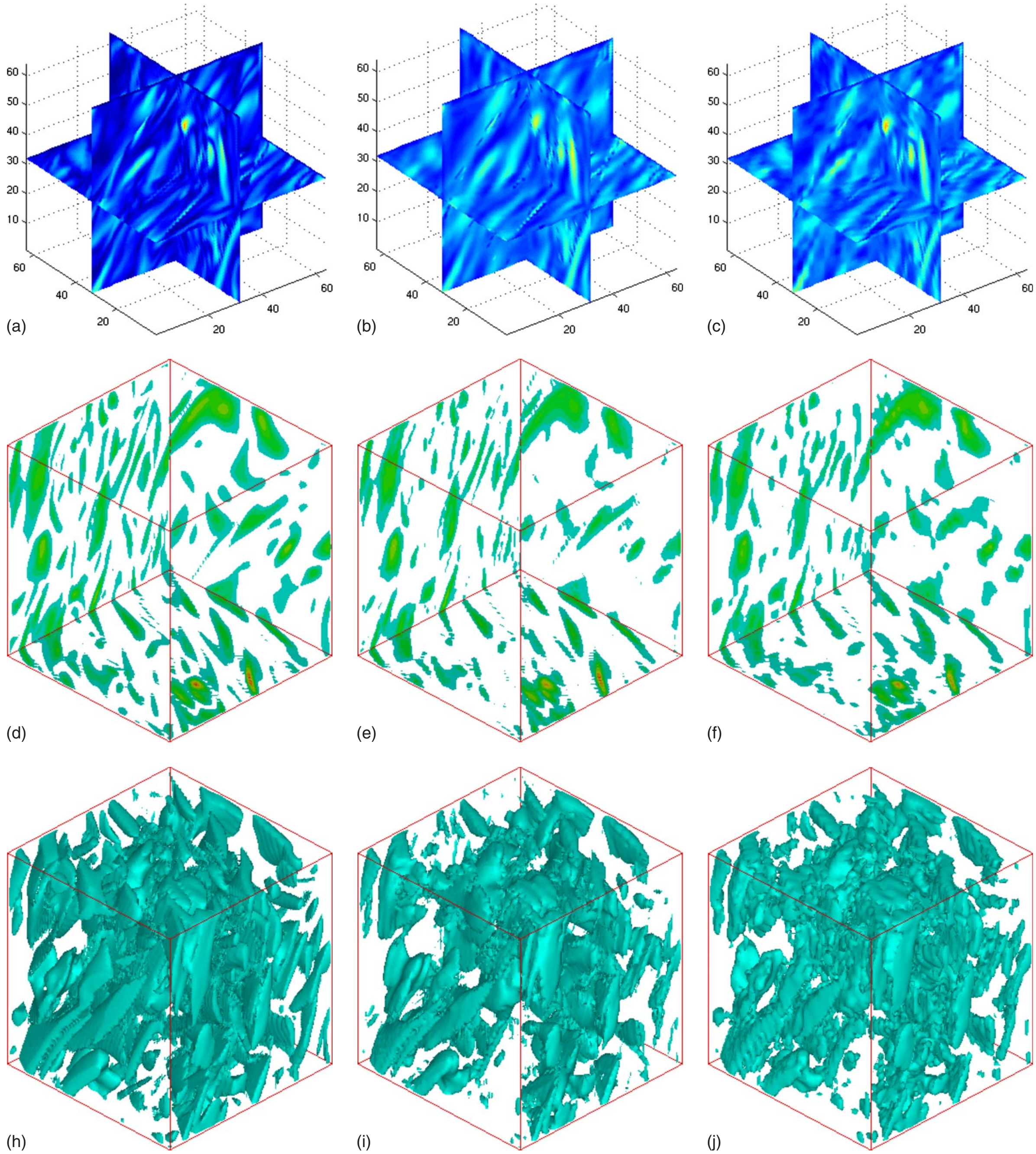

FIG. 18. (Color online) Partial reconstruction by curvelets and wavelets (left column). Total vorticity (middle column). Reconstruction using 1% of curvelet coefficients (right column). Reconstruction using 1% of wavelet coefficients. Different rows display the same results differently to highlight the clarity of the edges and structures using curvelets.

structures using curvelets preserve edges better than those obtained by wavelets. The oscillations along the edges, obvious in the figures of the right column, are due to the wavelet's deficiency in representing surface singularities. Quantitative analysis shows that the 1% of the largest curvelet and wavelet coefficients retains 97.3% and 95.0% of the total energy, respectively. Regarding the total enstrophy $\left(Z=\frac{1}{2}\int|\omega|^2dx\right)$ of the original flow, the curvelet- and wavelet-based reconstructions of vortices retain 95.8% and 97.1%, respectively. As can be clearly seen from the figure, the proposed curvelet method captures the total energy and enstrophy of the original flow as the wavelet method does but with better edges and structures.

The advantages of the proposed TV-synthesis iterative shrinkage are illustrated in Fig. 19. In this case we set a threshold to keep 0.05% of the coefficients, but all smooth coefficients at the coarsest scale are retained even whose values are smaller than the threshold. Figure 19 [(left) and (middle)] shows the wavelet reconstruction and curvelet reconstruction with a one-step hard threshold, respectively. The wavelet-filtered field results in oscillations along the edges, while the curvelets solve this problem with small remaining pseudo-Gibbs artifacts that are parallel to the edges. Figure 19 (right) is the reconstructed results using the TV-synthesis curvelet transform with step size of 0.015 and an iteration of 10.

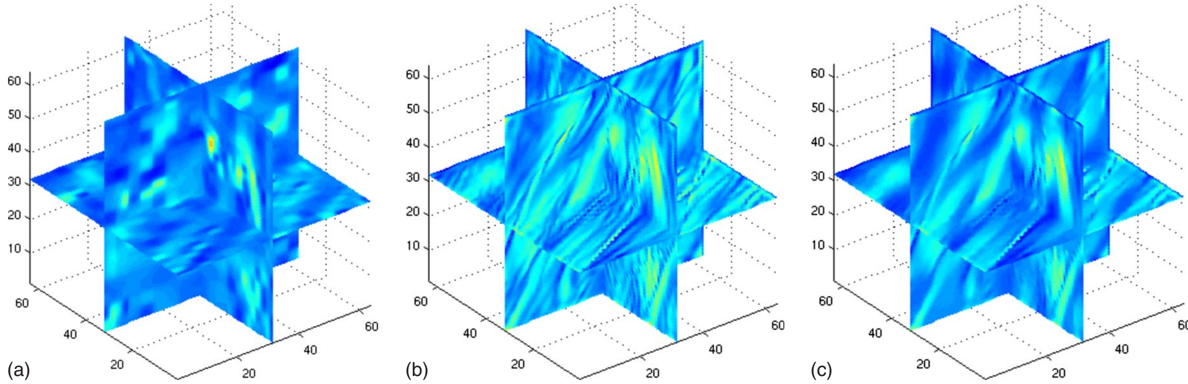

FIG. 19. (Color online) Thresholded reconstruction by wavelets (left), curvelets (middle), and the proposed TV-synthesis curvelet transform (right). The threshold is set to keep the 0.5% largest coefficients and the smooth coefficients at the coarsest scale are kept unchanged.

The corresponding isosurfaces are shown in Fig. 20. Figure 20(a) shows the original flow, and Fig. 20(b) shows the coherent components extracted by the wavelet transform. The 3D discontinuities are obvious. Figure 20(c) is the coherent components extracted by the curvelet transform. It can be seen that the edges/surfaces are preserved much better than the surface shown in Fig. 20(b). In Fig. 20(d), the result obtained by TV-synthesis curvelets further improves the curvelet's artifacts. We note that the same cut-off threshold of color is used in Figs. 20(a)–20(d). Figures 20(e) and 20(f) show the removed incoherent components by curvelets and TV-synthesis curvelets. We can see that more detailed oscillations are retained in the incoherent field by the curvelet method.

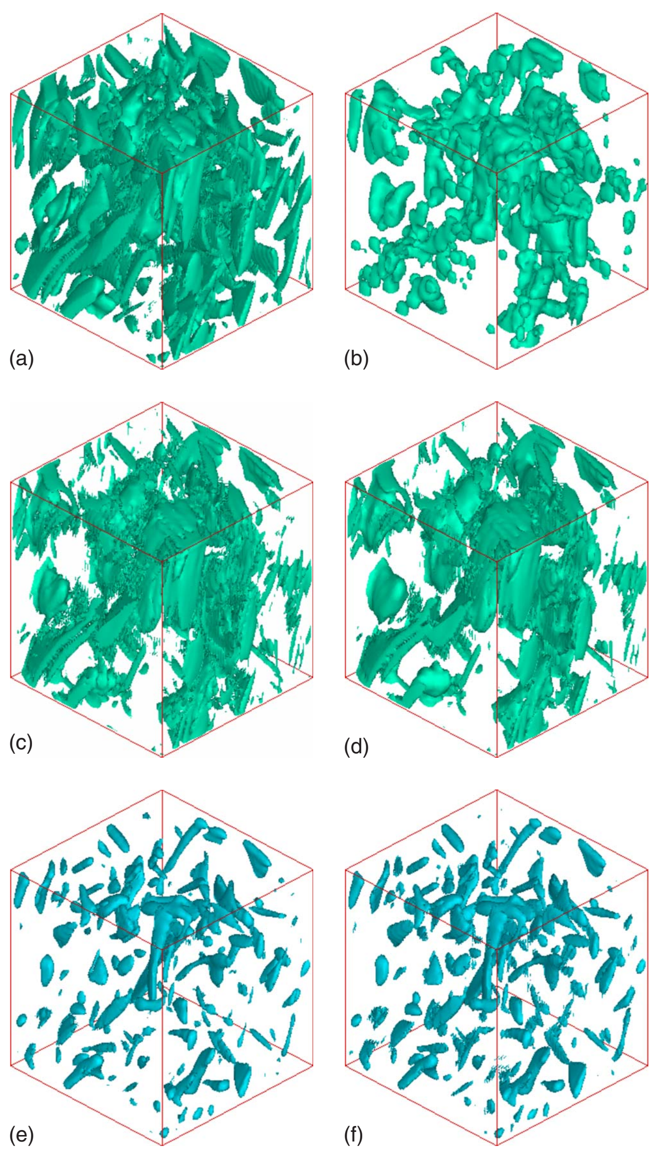

FIG. 20. (Color online) Extracted results shown in isosurface. (a) Original flow. (b) Coherent components by wavelets. (c) By curvelets. (d) By TV-synthesis curvelets. [(e) and (f)] Removed incoherent components by curvelets and TV-synthesis curvelets.

In order to further demonstrate that the curvelet filtered residual field is Gaussian, Fig. 21 shows the statistical analysis of the residual incoherent vorticity field both in linear and semilogarithmic scales. These results clearly demonstrate the ability of the curvelet transform to decompose a turbulent flow field into non-Gaussian coherent and incoherent fields with a probability density function similar to that of Gaussian distributions. Consequently, the curvelet transform can be used in the context of both CVS (Ref. 8) and SCALES.[5] Note that more experiments on the statistical analysis of 3D separated fields can be found in our previous work,[24] in which we observed that the coherent fields obtained by the curvelet and wavelet methods basically satisfy a gamma distribution, and the incoherent component nearly fits the Gaussian distribution. This is somewhat different from the previous observation using wavelets[9] that the component fields exhibit an exponential distribution, which is a special case of the gamma distribution.

Finally, we want to emphasize the physical significance of extracted structures by the proposed method. A puzzling feature of 3D turbulence is the large deviation from the Gaussian observed as one probes smaller and smaller scales.[58] These deviations are usually believed to be associated with spatial intermittency of small-scale structures, organized into very thin and elongated intense vortices. Energy containing eddies at a given scale interact with other eddies. Decomposing the turbulence into curvelet multiscale and multidirection domains is useful to determine the influence of the local and nonlocal interactions on the intermittency corrections in scaling properties. We observed that the similar spatial localization and direction of the structures are retained in successive scales. They vary in relative size from one filtered scale to the next. Tracking the changes in geometrical structures scale by scale (or subband by subband) is

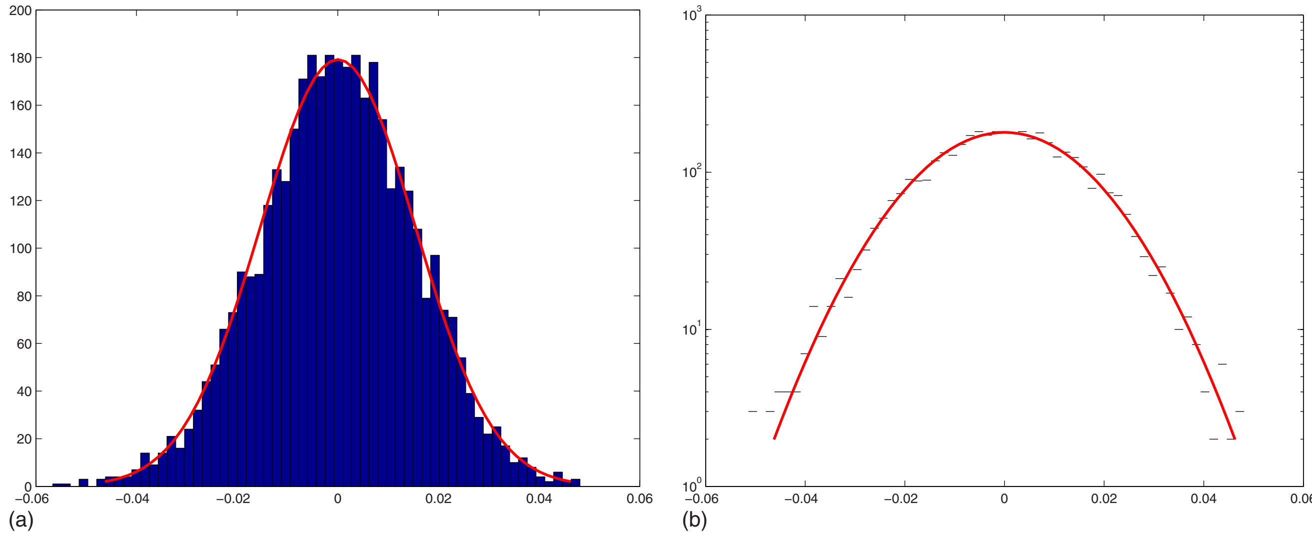

FIG. 21. (Color online) Statistical analysis for the residual field. (a) Histogram and its normal distribution fit. (b) Semilogarithmic display of (a). The solid line denotes Gaussian normal distribution.

helpful to understand the nonlocality and intermittency of turbulence. Another significance of the proposed method is to provide a potential filter in LES.

VIII. CONCLUSIONS

Turbulence is difficult to approximate and analyze mathematically or to calculate numerically because of its range of spatial and temporal scales. Vortical structures are essential characteristic features of turbulence. Vortex tube surface singularities underlie 3D turbulent flows. The development of appropriate tools to study vortex breakdown, vortex reconnection, turbulent entrainment at laminar-turbulent interfaces, etc., is imperative to enhance our understanding of turbulence. Such tools must capture vortical structure and dynamics accurately to unravel the physical mechanisms underlying these phenomena.

In this paper, the curvelet transform is applied to multiscale geometric analysis of turbulence in both two and three dimensions from laboratory data to DNS data. The MGA technique with curvelets as basis functions is verified as being effective for the extraction and compression of coherent structures underlying turbulent data. 3D TV-based curvelet shrinkage is proposed to suppress the pseudo-Gibbs artifacts, which also makes it possible to obtain incoherent Gaussian background flows easily where the classical theory of homogeneous turbulence involving Gaussian statistical equilibrium is valid. The turbulence analysis is posed as an optimization problem involving the TV norm and a constraint on the curvelet space. The curvelet method is also promising to get a high compression number of spatial modes to simulate large Reynolds numbers of practical interest. This method can also be applied to other fields.

There is room for future research to further explore the application of curvelets and TV regularization in turbulence. Like other filtering methods, such as wavelets, the results are dependent on the threshold or shrinkage. The question of how to find the optimal threshold still remains open. It must also be mentioned that the computational cost of curvelets is higher than that of wavelets. However, the theory and application of 3D curvelets are burgeoning areas of research, and it is possible that more efficient curvelet transforms will be developed in the near future. Currently, a fast message passing interface-based parallel implementation can somewhat reduce the cost.[23]

A natural extension is a CVS or SCALES of turbulent flows based on the curvelet-based coherent vortex extraction and adaptive computation,[5,59,60] which is the subject of our continuing work. To develop and apply an orthogonal curvelet transform is another direction of future work.

ACKNOWLEDGMENTS

J.M. gratefully acknowledges the financial support by NSFC under Grant No. 40704019 and the hospitality of the Florida State University and the University of Colorado at Boulder, without which this work could not have been completed. O.V.V. was partially supported by the Department of Energy (DOE) under Grant No. DE-FG02-05ER25667.

[1] T. B. Gatski, M. Y. Hussaini, and J. L. Lumley, *Simulation and Modeling of Turbulent Flows* (Oxford University Press, Oxford, 1996).
[2] C. Meneveau and J. Katz, “Scale-invariance and turbulence models for large-eddy simulation,” Annu. Rev. Fluid Mech. **32**, 1 (2000).
[3] P. Moin, “Advances in large eddy simulation methodology of complex flows,” Int. J. Heat Fluid Flow **23**, 710 (2002).
[4] M. Farge and K. Schneider, “Coherent vortex simulation (CVS), a semideterministic turbulence model using wavelets,” Flow, Turbul. Combust. **66**, 393 (2001).
[5] D. Goldstein and O. V. Vasilyev, “Stochastic coherent adaptive large eddy simulation method,” Phys. Fluids **16**, 2497 (2004).
[6] P. Sagaut, S. Deck, and M. Terracol, *Multiscale and Multiresolution Approaches in Turbulence* (Imperial College Press, London, 2006).
[7] M. Farge, “Wavelet transforms and their applications to turbulence,” Annu. Rev. Fluid Mech. **24**, 395 (1992).
[8] M. Farge, K. Schneider, and N. Kevlahan, “Non-Gaussiannity and coherent vortex simulation for two-dimensional turbulence suing an adaptive orthonormal wavelet basis,” Phys. Fluids **11**, 2187 (1999).
[9] M. Farge, G. Pellegrino, and K. Schneider, “Coherent vortex extraction in 3D turbulent flows using orthogonal wavelets,” Phys. Rev. Lett. **87**, 054501 (2001).

[10]M. Farge, E. Goirand, Y. Meyer, F. Pascal, and M. Wickerhauser, "Improved predictability of two-dimensional turbulent flows using wavelet packet compression," Fluid Dyn. Res. **10**, 229 (1992).
[11]P. Fischer, "Multiresolution analysis for 2D turbulence. Part 1: Wavelets vs cosine packets, a comparative study," Discrete Contin. Dyn. Syst., Ser. B **5**, 659 (2005).
[12]O. Roussel, K. Schneider, and M. Farge, "Coherent vortex extraction in 3D homogeneous turbulence: Comparison between orthogonal and biorthogonal wavelet decompositions," J. Turbul. **6**, 11 (2005).
[13]D. Goldstein, O. V. Vasilyev, and N. K. Kevlahan, "CVS and SCALES simulation of 3D isotropic turbulence," J. Turbul. **6**, 37 (2005).
[14]J. Qiu, K. T. Paw U, and R. Shaw, "The leakage problem of orthonormal wavelet transforms when applied to atmospheric turbulence," J. Geophys. Res. **100**, 25769, DOI:10.1029/95JD02596 (1995).
[15]E. J. Candès and D. L. Donoho, "Curvelets—a surprisingly effective nonadaptive representation for objects with edges," in *Curves and Surface Fitting: Saint-Malo 1999*, edited by A. Cohen, C. Rabut, and L. Schumaker (Vanderbilt University Press, Nashville, 2000), pp. 105–120.
[16]E. J. Candès and D. L. Donoho, "New tight frames of curvelets and optimal representations of objects with piecewise C^2 singularities," Commun. Pure Appl. Math. **57**, 219 (2004).
[17]E. J. Candès, L. Demanet, D. L. Donoho, and L. Ying, "Fast discrete curvelet transforms," Multiscale Model. Simul. **5**, 861 (2006).
[18]J. Ma, A. Antoniadis, and F.-X. Le Dimet, "Curvelet-based snake for multiscale detection and tracking of geophysical fluids," IEEE Trans. Geosci. Remote Sens. **44**, 3626 (2006).
[19]J. Ma and G. Plonka, "Combined curvelet shrinkage and nonlinear anisotropic diffusion," IEEE Trans. Image Process. **16**, 2198 (2007).
[20]J. Ma, "Curvelets for surface characterization," Appl. Phys. Lett. **90**, 054109 (2007).
[21]J. L. Starck, E. J. Candès, and D. L. Donoho, "The curvelet transform for image denoising," IEEE Trans. Image Process. **11**, 670 (2002).
[22]J. L. Starck, E. J. Candès, and D. L. Donoho, "Astronomical image representation by the curvelet transform," Astron. Astrophys. **398**, 785 (2003).
[23]L. Ying, L. Demanet, and E. Candès, "3D discrete curvelet transform," Proc. SPIE **5914**, 591413 (2005).
[24]J. Ma and M. Y. Hussaini, "Three-dimensional curvelets for coherent vortex analysis of turbulence," Appl. Phys. Lett. **91**, 184101 (2007).
[25]I. Bermejo-Moreno and D. Pullin, "On the non-local geometry of turbulence," J. Fluid Mech. **603**, 101 (2008).
[26]F. Fernandes, "Directional, shift-insensitive, complex wavelet transforms with controllable redundancy," Ph.D. thesis, Rice University, 2001.
[27]X. Gao, T. Nguyen, and G. Strang, "A study of two-channel complex-valued filterbanks and wavelets with orthogonality and symmetry properties," IEEE Trans. Signal Process. **50**, 824 (2002).
[28]N. Kingsbury, "Image processing with complex wavelets," Philos. Trans. R. Soc. London, Ser. A **357**, 2543 (1999).
[29]N. Kingsbury, "Complex wavelets for shift invariant analysis and filtering of signals," Appl. Comput. Harmon. Anal. **10**, 234 (2001).
[30]E. Candès, "Harmonic analysis of neural networks," Appl. Comput. Harmon. Anal. **6**, 197 (1999).
[31]E. Candès and D. Donoho, "Ridgelets: A key to higher-dimensional intermittency?" Philos. Trans. R. Soc. London, Ser. A **357**, 2495 (1999).
[32]J. Ma and M. Fenn, "Combined complex ridgelet shrinkage and total variation minimization," SIAM J. Sci. Comput. (USA) **28**, 984 (2006).
[33]D. Donoho, "Wedgelets: Nearly minimax estimation of edges," Ann. Stat. **27**, 859 (1999).
[34]D. Donoho and X. Huo, "Beamlets and multiscale image analysis," in *Multiscale and Multiresolution Methods*, Springer Lecture Notes in Computational Science and Engineering, edited by T. Barth, T. Chan, and R. Haimes (Springer, New York, 2002), Vol. 20, pp. 149–196.
[35]S. Mallat and G. Peyré, "A review of bandlet methods for geometrical image representation," Numer. Algorithms **44**, 205 (2007).
[36]E. Le Pennec and S. Mallat, "Sparse geometric image representations with bandlets," IEEE Trans. Image Process. **14**, 423 (2005).
[37]M. Do and M. Vetterli, "The contourlet transform: An efficient directional multiresolution image representation," IEEE Trans. Image Process. **14**, 2091 (2005).
[38]K. Guo and D. Labate, "Optimally sparse multidimensional representation using shearlets," SIAM J. Math. Anal. **39**, 298 (2007).
[39]R. Willett and K. Nowak, "Platelets: A multiscale approach for recovering edges and surfaces in photon-limited medical imaging," IEEE Trans. Med. Imaging **22**, 332 (2003).
[40]Y. Lu and M. N. Do, "Multidimensional directional filter banks and surfacelets," IEEE Trans. Image Process. **16**, 918 (2007).
[41]J. Weickert, "Coherence-enhancing diffusion filtering," Int. J. Comput. Vis. **31**, 111 (1999).
[42]I. Daubechies, *Ten Lectures on Wavelets* (SIAM, Philadelphia, PA, 1992).
[43]M. Farge, N. Kevlahan, V. Perrier, and E. Goirand, "Wavelets and turbulence," Proc. IEEE **84**, 639 (1996).
[44]B. Cantwell, "Organized motion in turbulent flow," Annu. Rev. Fluid Mech. **13**, 457 (1981).
[45]A. F. Hussain, "Coherent structures and turbulence," J. Fluid Mech. **173**, 303 (1986).
[46]G. De Stefano, D. E. Goldstein, and O. V. Vasilyev, "On the role of subgrid-scale coherent modes in large-eddy simulation," J. Fluid Mech. **525**, 263 (2005).
[47]G. De Stefano and O. V. Vasilyev, "Sharp cutoff versus smooth filtering in large eddy simulation," Phys. Fluids **14**, 362 (2002).
[48]G. De Stefano and O. V. Vasilyev, "Perfect modeling framework for dynamic SGS model testing in large eddy simulation," Theor. Comput. Fluid Dyn. **18**, 27 (2004).
[49]O. V. Vasilyev, T. Lund, and P. Moin, "A general class of commutative filters for LES in complex geometries," J. Comput. Phys. **146**, 82 (1998).
[50]K. Schneider, M. Farge, A. Azzalini, and J. Ziuber, "Coherent vortex extraction and simulation of 2D isotropic turbulence," J. Turbul. **7**, 44 (2006).
[51]D. Donoho and I. Johnstone, "Ideal spatial adaptation via wavelet shrinkage," Biometrika **81**, 425 (1994).
[52]S. Durand and J. Froment, "Reconstruction of wavelet coefficients using total variation minimization," SIAM J. Sci. Comput. (USA) **24**, 1754 (2003).
[53]J. Ma, "Characterization of textual surfaces using wave atoms," Appl. Phys. Lett. **90**, 264101 (2007).
[54]L. Rudin, S. Osher, and E. Fatemi, "Nonlinear total variation based noise removal algorithms," Physica D **60**, 259 (1992).
[55]G. Steidl, J. Weickert, T. Brox, P. Mrázek, and M. Welk, "On the equivalence of soft wavelet shrinkage, total variation diffusion, total variation regularization, and SIDEs," SIAM (Soc. Ind. Appl. Math.) J. Numer. Anal. **42**, 686 (2004).
[56]I. Selesnick, S. Cai, and K. Li, "Matlab implementation of wavelet transforms," URL: http://taco.poly.edu/WaveletSoftware/.
[57]R. Samtaney, D. I. Pullin, and B. Kosović, "Graduate direct numerical simulation of decaying compressible turbulence and shocklet statistics," Phys. Fluids **13**, 1415 (2001).
[58]J. Laval, B. Dubrulle, and S. Nazarenko, "Nonlocality and intermittency in three-dimensional turbulence," Phys. Fluids **13**, 1995 (2001).
[59]J. Ma, G. Tang, and M. Y. Hussaini, "A refining estimation for adaptive solution of wave equation based on curvelets," Proc. SPIE **6701**, 67012J (2007).
[60]O. V. Vasilyev, "Solving multi-dimensional evolution problems with localized structures using second generation wavelets," Int. J. Comput. Fluid Dyn. **17**, 151 (2003).